Acta Astronautica 212 (2023) 672–685

Contents lists available at ScienceDirect

Acta Astronautica

journal homepage: www.elsevier.com/locate/actaastro

Lunar descent and landing via two-phase explicit guidance and pulse-modulated reduced-attitude control

Mauro Pontani [a,b,*], Fabio Celani [c,a], Stefano Carletta [c,a]

[a] Sapienza Università di Roma, 00138, Rome, Italy
[b] Department of Astronautical, Electrical, and Energy Engineering, Via Salaria 851, Italy
[c] School of Aeropace Engineering, Via Salaria 851, Italy

ARTICLE INFO

Keywords:
Lunar descent and landing
Autonomous explicit guidance
Reduced-attitude control
Pulse width modulation
Planetary probes

ABSTRACT

This work considers the three-dimensional descent path of a space vehicle, from periselenium of its operational orbit to the lunar surface. The trajectory is split in two arcs: (1) descent path, up to an altitude of 50 m, and (2) terminal approach and soft touchdown. For phase 1, a new, three-dimensional locally-flat near-optimal guidance is introduced that is based on the local projection of the position and velocity variables. A minimum-time problem is defined using the locally flat coordinates of position and velocity. This leads to identifying closed-form functions of time for the two thrust angles, which identify the commanded thrust direction. During terminal approach (phase 2), correct vertical alignment, modest velocity, and negligible angular rate at touchdown are pursued. With this intent, a predictive bang-off-bang guidance algorithm is proposed that is capable of guaranteeing the desired final conditions. In both phases, the attitude control system has the objective of aligning the actual thrust direction with the commanded one, provided by the guidance algorithm. The resulting reduced-attitude control problem is addressed through the use of a new quaternion-based nonlinear control algorithm, which is proven to enjoy asymptotic stability properties. The attitude actuation system is composed of 12 monopropellant thrusters, ignited using pulse width modulation. Monte Carlo simulations are run, assuming significant displacements from the nominal initial conditions and including several harmonics of the selenopotential. The numerical results unequivocally prove that the guidance and control architecture proposed in this study is effective to achieve lunar descent and safe touchdown in nonnominal flight conditions.

1. Introduction

In recent years, human and robotic missions to the Moon are attracting a renewed interest by the scientific community, and some lunar missions are planned in this decade. The development of a safe and reliable guidance and control architecture for autonomous lunar descent and soft touchdown represents a challenging and crucial issue for enabling in situ operations, with the perspective of establishing a permanent lunar settlement. The bulk of the work on lunar landing dates back to the early years of the Apollo missions [1], with the original work by Klumpp, who implemented an explicit guidance, known as the E-guidance [2]. Significant advances in the computational capabilities occurred since the conclusion of the Apollo program, and allowed adapting Apollo-class guidance to autonomous real-time operations [3,4]. Recent contributions on the study of guidance and control techniques tailored to lunar descent and touchdown are due to Chomel and Bishop [5], who proposed a targeting algorithm based on generating a two-dimensional trajectory, used as a reference for three-dimensional guidance. Later, Azimov and Bishop [6] developed an on-board guidance and targeting algorithm based on the closed-form analytical solution for the touchdown phase assuming constant thrust. These algorithms are characterized by a large propellant usage, which could limit their implementation. Related to this issue, Lee [7] assumed a continuous time-varying thrust profile and referred to a nominal trajectory similar to that used in the Apollo 11 mission, capable of guaranteeing safe touchdown conditions, together with acceptable fuel consumption. Reynolds and Mesbahi [8] further investigated the powered descent problem, assuming a maneuver that evolves onto an inertially fixed plane, with the inclusion of the effects of an independent torque input and constraints on the thrust magnitude. Other publications focused on descent paths, obtained by means of either artificial intelligence techniques [9] or shooting methods [10]. In particular, Hull

* Corresponding author. Department of Astronautical, Electrical, and Energy Engineering, Via Salaria 851, Italy
E-mail address: mauro.pontani@uniroma1.it (M. Pontani).

https://doi.org/10.1016/j.actaastro.2023.07.026
Received 17 October 2022; Received in revised form 14 July 2023; Accepted 22 July 2023
Available online 25 July 2023

[10] investigated optimal guidance for quasi-planar lunar descent with thrust throttling over a flat Moon. Zhang and Duan [11] developed an integrated translational and rotational strategy, formulated as a filter-based backstepping control, and implemented some effective solutions to overcome numerical singularities. Ma et al. [12] investigated the translational dynamics in the three-dimensional descent problem, and proposed fuel-optimal solutions through dynamic optimization based on mesh refinement. Mathavaraj et al. [13] studied the three-dimensional descent problem as well, while neglecting attitude dynamics, and solved it by using the Legendre pseudospectral method. Cortés-Martínez et al. [14] identified a solution for three-dimensional lunar descent, using a six-degree-of-freedom model for a spacecraft equipped with a gimballed thruster and designing a feedback law with optimal control gains. Zhukov et al. [15] proposed a proportional guidance descent-control algorithm, based on the free-fall braking maneuver, which allows selecting the landing place on the lunar surface and the touchdown velocity, whereas Andrew et al. [16] extended the use of convex optimization to lunar landing with several constraints. In the majority of works focused on lunar descent, the design of guidance and control algorithms is carried out separately, by exploiting time scale separation. A possible different approach is executing an integrated guidance and control design as in Refs. [17,18], focused on atmospheric entry. Finally, some mission-oriented works dealt with effective terrain-relative navigation techniques [19,20], able to provide the measurements needed for successful touchdown and (eventually) hazard detection and avoidance [21–23].

This research considers the three-dimensional descent path of a spacecraft, from periselenium of its operational orbit to the lunar surface. The gravitational model includes several relevant harmonics of the selenopotential. The landing vehicle is equipped with a main propulsion system, for trajectory control, accompanied by 12 monopropellant thrusters, equally distributed into three mutually orthogonal planes and mainly dedicated to attitude maneuvering. The trajectory is split in two arcs: (1) descent trajectory, up to an altitude of 50 m, and (2) terminal approach and soft touchdown. For phase 1, a new, three-dimensional locally-flat near-optimal guidance is introduced that is based on the local projection of the position and velocity variables. A minimum-time problem is defined using the locally flat coordinates of position and velocity. During terminal approach (phase 2), correct vertical alignment, modest velocity, and negligible angular rate at touchdown are pursued. With this intent, a predictive bang-off-bang guidance algorithm is proposed, aimed at guaranteeing the desired final conditions, while providing the proper allocation of side jet ignitions. In both phases 1 and 2, the attitude control system has the objective of aligning the actual thrust direction, which is fixed with respect to the spacecraft, with the commanded one, provided by the guidance algorithm. Thus, for the problem at hand, attitude control must pursue single-axis alignment, which is also known in the literature as reduced-attitude control. Significant contributions on reduced-attitude control can be found in Ref. [24], focused on pointing control with respect to an inertially fixed direction, and in Refs. [25,26], which consider reduced-attitude-tracking, corresponding to the more general situation of a desired time-varying pointing direction. The latter two works describe feedback laws that enjoy asymptotic convergence properties. This work presents and applies a new quaternion-based nonlinear reduced-attitude control algorithm, which is intended to pursue a time-varying direction. The attitude actuation system consists of 12 monopropellant thrusters, equally distributed into three mutually orthogonal planes. They are ignited using pulse width modulation [27–29]. This study represents a considerable extension of previous research by the same authors [30], focused on planar descent and touchdown. In fact, this work considers perturbed three-dimensional trajectories, which is a more realistic description of the actual mission scenario with respect to perturbed planar paths (assumed in Ref. [30]). This circumstance leads to the following major novelties with respect to previous research [30]. First, the guidance algorithms in phases 1 and 2 extend the preceding schemes developed for planar descent paths. Second, attitude control employs a completely different, original, quaternion-based feedback law, aimed at aligning the spacecraft longitudinal axis with a desired time-varying direction. Third, actuation is achieved using a more complex system that includes 12 side jets.

In short, the primary objectives of this research are (i) the introduction and description of two original guidance techniques for the two phases of the three-dimensional descent path, (ii) the definition and stability analysis of a novel quaternion-based nonlinear reduced-attitude control algorithm, capable of identifying a feedback attitude control law, (iii) the implementation of a guidance, control, and actuation architecture that includes pulse width modulation for igniting the side jet thrusters, and (iv) the numerical testing of the previously mentioned guidance, control, and actuation architecture, in the presence of non-nominal flight conditions.

2. Spacecraft dynamics

The Peregrine lander, whose design is described in Ref. [31], is selected as the prototypical vehicle model. Although its geometry is more complex, it can be modeled as a cylinder, with diameter D of 2 m and height of 2 m. Its initial mass and principal inertia moments with respect to the center of mass equal $m_0 = 1283$ kg, $I_{xx,0} = 1827\text{kg m}^2$, and $I_{yy,0} = I_{zz,0} = 819\text{kg m}^2$. The space vehicle at hand is assumed to be equipped with a main thruster, aligned with the longitudinal axis, and 12 side jets, in the configuration illustrated in Fig. 1. The main thruster provides a constant thrust with magnitude T = 4730 N. Each monopropellant side jet supplies a thrust whose magnitude F_{tot} equals 200 N at the initial time t_i, and decreases exponentially due to pressurant depletion [32], i.e. $F_{tot}(t) = F_{tot}(t_i)\exp[-(t-t_i)/t_{car}]$, where t_{car} equals to 7027 s. The time constant t_{car} is a characteristic parameter that depends on the tank volume, the pressurization system, and the fluid properties [33].

Besides thrust, the descent vehicle is assumed to be subject only to the gravitational attraction of the Moon. The mass ratio, denoted with $x_7 = m/m_0$, obeys

$$\dot{x}_7 = -\frac{n_T}{c_M} - \frac{n_{SJ}}{c_{SJ}} \tag{1}$$

where $n_T := T/m_0$ and $n_{SJ} := F_{tot}/m_0$; c_M (= 3 km/sec) and c_{SJ} (= 2.158 km/sec) are the effective exhaust velocities of the main thruster and the side jets, respectively. While n_T is constant, n_{SJ} reduces due to decrease of F_{tot}. Trajectory and attitude equations, reported in the next subsections, govern the spacecraft dynamics.

2.1. Trajectory

The descent trajectory is described in an inertial reference frame, associated with the right-hand sequence of unit vectors $(\hat{c}_1, \hat{c}_2, \hat{c}_3)$. Its origin is located at the center of the Moon, and the initial elliptic orbit lies on the $(\hat{c}_1, \hat{c}_2)$-plane, with periselenium aligned with $\hat{c}_1$. The position can be identified by the following three variables: radius r right ascension ξ, and declination φ, portrayed in Fig. 2(a). The spacecraft velocity can be projected into the rotating frame $(\hat{r}, \hat{t}, \hat{n})$, where $\hat{r}$ is aligned with the position vector $\underrightarrow{\mathbf{r}}$ and $\hat{t}$ is parallel to the $(\hat{c}_1, \hat{c}_2)$-plane (and in the direction of the spacecraft motion, cf. Fig. 2(a)). The related components are denoted with (v_r, v_t, v_n) and termed respectively radial, transverse, and normal velocity component. The lander trajectory is controlled through the thrust direction, defined by the in-plane angle α and the out-of-plane angle β, both illustrated in Fig. 2(b) (in which $\hat{T}$ is aligned with the thrust direction).

The trajectory equations govern the time evolution of x_7 (cf. Eq. (1)) and $(r, \xi, \varphi, v_r, v_t, v_n)$,

$$\dot{r} = v_r \tag{2}$$

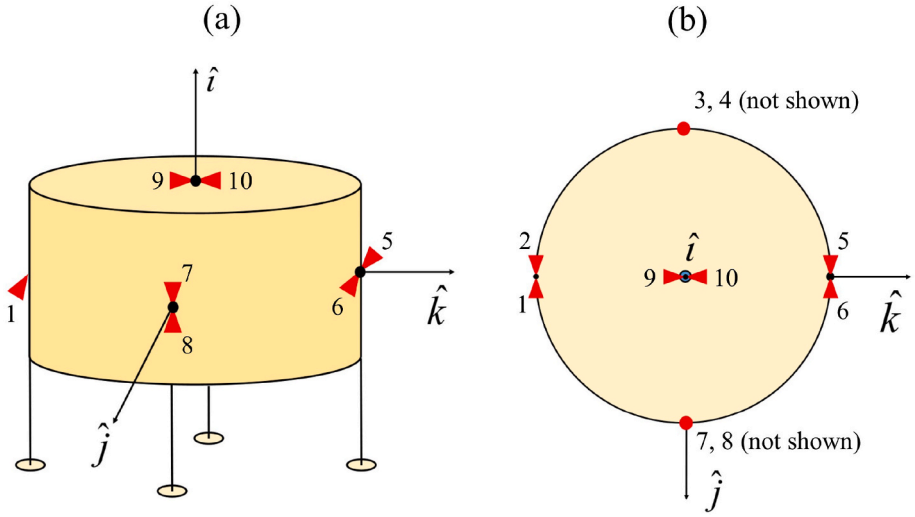

Fig. 1. Illustrative sketch of the lander and the 12-side-jet arrangement: (a) 3-d view (b) top view.

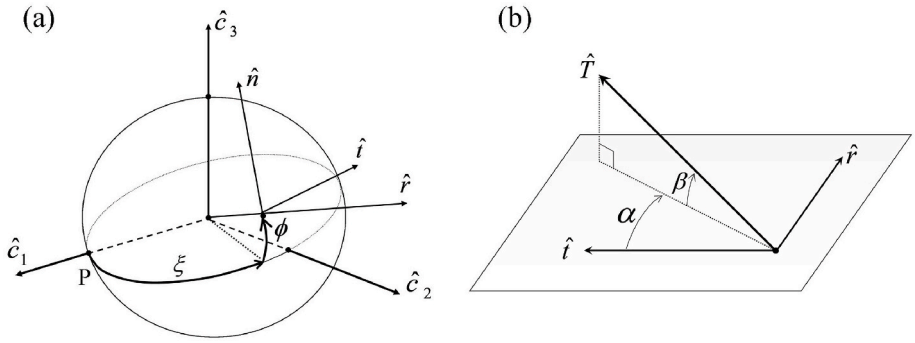

Fig. 2. Reference frames (a) and thrust angles **α** and **β** (b).

$$\dot{\xi} = \frac{v_t}{r\cos\varphi} \tag{3}$$

$$\dot{\varphi} = \frac{v_n}{r} \tag{4}$$

$$\dot{v}_r = -\frac{\mu}{r^2} + \frac{v_t^2 + v_n^2}{r} + a_T \sin\alpha\cos\beta + a_{P,r} \tag{5}$$

$$\dot{v}_t = \frac{v_t}{r}(v_n \tan\varphi - v_r) + a_T \cos\alpha\cos\beta + a_{P,t} \tag{6}$$

$$\dot{v}_n = -\frac{v_t^2}{r}\tan\varphi - \frac{v_r v_n}{r} + a_T \sin\beta + a_{P,n} \tag{7}$$

where $a_T\ (= n_T/x_7)$ is the instantaneous thrust acceleration, $\mu\ (= 4903\ \mathrm{km^3/sec^2})$ is the lunar gravitational parameter, whereas $(a_{P,r}, a_{P,t}, a_{P,n})$ represent the three components of the perturbing acceleration. In this research, all the zonal harmonics of the selenopotential with $|J_l| > 10^{-6}$ are included, i.e. $J_2, J_3, J_4, J_6, J_7, J_8, J_9, J_{11}, J_{12}, J_{17}, J_{28}$, and J_{29}, taken from the Lunar Prospector LPE100K model. Moreover, the $(\hat{c}_1, \hat{c}_2)$-plane is assumed to coincide with the lunar equatorial plane. As a result, the transverse and normal components (of velocity and acceleration) are identical to the respective East and North components.

2.2. Attitude

The spacecraft is modeled as a rigid body and its instantaneous orientation is associated with the body frame. Its axes are aligned with the right-hand sequence of unit vectors $(\hat{\imath}, \hat{\jmath}, \hat{k})$, with $\hat{\imath}$ pointing toward the longitudinal axis of the lander. Vectrix $\underline{\underline{B}}$ is composed of $(\hat{\imath}, \hat{\jmath}, \hat{k})$, i.e. $\underline{\underline{B}} := [\hat{\imath}\ \ \hat{\jmath}\ \ \hat{k}]$; similarly, the right-hand sequence $(\hat{c}_1, \hat{c}_2, \hat{c}_3)$, corresponding to the inertial frame, forms vectrix $\underline{\underline{N}} := [\hat{c}_1\ \ \hat{c}_2\ \ \hat{c}_3]$.

In this research, the instantaneous attitude is referred to $\underline{\underline{N}}$ and is described through Euler parameters (quaternions), denoted with $\{q_0, \mathbf{q}\}$, where q_0 is the scalar part, whereas $\mathbf{q}$ is the (3×1)-vector part. If $^{N}\underrightarrow{\boldsymbol{\omega}}^{B}$ denotes the vector angular rate of $\underline{\underline{B}}$ with respect to $^{N}\underrightarrow{\boldsymbol{\omega}}^{B}$, the attitude kinematics equations are [34]

$$\dot{q}_0 = -\frac{1}{2}\mathbf{q}^T\boldsymbol{\omega} \tag{8}$$

$$\dot{\mathbf{q}} = \frac{1}{2}[q_0\mathbf{I}_{3\times 3} + \tilde{\mathbf{q}}]\boldsymbol{\omega} \tag{9}$$

where $\boldsymbol{\omega}$ denotes the (3×1)-vector that contains the three components of $^{N}\underrightarrow{\boldsymbol{\omega}}^{B}$ in $\underline{\underline{B}}$, i.e. $^{N}\underrightarrow{\boldsymbol{\omega}}^{B} = \underline{\underline{B}}\boldsymbol{\omega}$, $\tilde{\mathbf{q}}$ is the skew-symmetric matrix associated with $\mathbf{q}$, and $\mathbf{I}_{3\times 3}$ is the (3×3) identity matrix.

Under the (approximating) assumption that the mass center C is a fixed point inside the spacecraft during the entire time of flight, the attitude dynamics equations are decoupled from the trajectory equations, and involve the spacecraft angular momentum with respect to C, $\underrightarrow{\mathbf{H}}_C$. If $\mathbf{H}_C$ denotes the (3×1)-vector that includes the three components of $\underrightarrow{\mathbf{H}}_C$ in $\underline{\underline{B}}$, then [34]

$$\dot{\mathbf{H}}_C = -\tilde{\boldsymbol{\omega}}\mathbf{H}_C + \mathbf{M}_C + \mathbf{T}_C \tag{10}$$

where $\widetilde{\boldsymbol{\omega}}$ denotes the skew-symmetric matrix associated with $\boldsymbol{\omega}$, whereas $\mathbf{M}_C$ and $\mathbf{T}_C$ are (3×1)-vectors that include respectively the components (in $\underline{B}$) of the external torque and the control torque (supplied by the side jets). Let $\mathbf{J}_C^{(B)}$ denote the spacecraft inertia matrix with respect to C, resolved in $\underline{B}$. Because $\mathbf{H}_C = \mathbf{J}_C^{(B)}\boldsymbol{\omega}$, Eq. (10) becomes

$$\dot{\boldsymbol{\omega}} = \left[\mathbf{J}_C^{(B)}\right]^{-1}\left(-\widetilde{\boldsymbol{\omega}}\mathbf{J}_C^{(B)}\boldsymbol{\omega} - \dot{\mathbf{J}}_C^{(B)}\boldsymbol{\omega} + \mathbf{M}_C + \mathbf{T}_C\right) \tag{11}$$

In Eq. (11), $\dot{\mathbf{J}}_C^{(B)}$ is the time derivative of the inertia matrix, which is nonzero due to propellant consumption. In this research, homogeneous mass depletion is assumed to obtain $\dot{\mathbf{J}}_C^{(B)}$. External disturbing torques, such as that due to gravity gradient, are modest if compared to the control torque provided by the side jets (in fact, they differ by several orders of magnitude). This circumstance justifies the assumption that $\mathbf{M}_C$ is negligible for the problem at hand. Thus, $\mathbf{M}_C = \mathbf{0}$ hence forward. In the end, the nonlinear differential system composed of Eqs. (8), (9) and (11) govern the instantaneous attitude and angular rate of the spacecraft. The torque components of $\mathbf{T}_C$ represent the control input.

3. Phase 1. locally-flat near-optimal guidance

The descent path is split into two arcs: (1) approach phase, starting from periselenium of the lunar orbit and ending with zero velocity at a specified altitude h_i ($h_i = 50$ m, in this study), and (2) final descent and touchdown, from altitude h_i to the lunar surface. The junction condition corresponds to hovering at modest altitude. This allows checking the spacecraft instrumentation and instantaneous flight conditions, and facilitates the design of an abort maneuver, in the presence of unfavorable contingencies. Phase 1 is much longer than arc 2; nevertheless, phase 2 is crucial for the purpose of attaining the desired conditions at touchdown, i.e. vertical velocity magnitude not exceeding a limiting value (set to 1 m/s), zero horizontal velocity, longitudinal axis aligned with the vertical direction, and zero angular velocity. In particular, the preceding limiting value for the vertical velocity is half of the nominal vertical velocity of the Apollo modules [35]. Two distinct algorithms are proposed in this work for the two trajectory arcs. This section is focused on phase 1.

3.1. Local projection of position and velocity

For the approach phase 1, this research proposes a near-optimal guidance scheme based on local projection of the spacecraft position and velocity. The guidance algorithm is run repeatedly and starts at equally-spaced discrete times $\{t_k\}_{k=0,\ldots,N-1}$. The symbol Δt_S denotes the sampling time interval, i.e. $\Delta t_S = t_{k+1} - t_k$ $(k = 1,\ldots,N-2)$; the last interval is shorter, because the guidance and control algorithm stops when the desired conditions are reached with satisfactory accuracy. At time t_k, the spacecraft position and velocity $\underrightarrow{\mathbf{r}}$ and $\underrightarrow{\mathbf{v}}$ are denoted with $\underrightarrow{\mathbf{r}}_k$ and $\underrightarrow{\mathbf{v}}_k$, and are associated with $(r_k, \xi_k, \varphi_k, v_{r,k}, v_{t,k}, v_{n,k})$ and $(\hat{r}_k, \hat{t}_k, \hat{n}_k)$ (i.e., $(\hat{r}, \hat{t}, \hat{n})$ at t_k, cf. Fig. 2(b)). Let $(\hat{x}_k, \hat{y}_k, \hat{z}_k)$ denote three unit vectors obtained from $(\hat{r}_k, \hat{t}_k, \hat{n}_k)$ through a counterclockwise rotation about axis 2 b y angle φ_k. Vectors $\underrightarrow{\mathbf{r}}_k$ and $\underrightarrow{\mathbf{v}}_k$ are projected along $(\hat{x}_k, \hat{y}_k, \hat{z}_k)$,

$$\underrightarrow{\mathbf{r}}_k = r_k[\cos\varphi_k \quad 0 \quad \sin\varphi_k][\hat{x}_k \quad \hat{y}_k \quad \hat{z}_k]^T \tag{12}$$

$$\underrightarrow{\mathbf{v}}_k = [v_{r,k} \quad v_{t,k} \quad v_{n,k}]\mathbf{R}_2(-\varphi_k)\begin{bmatrix}\hat{x}_k\\ \hat{y}_k\\ \hat{z}_k\end{bmatrix} = \begin{bmatrix}v_{r,k}\cos\varphi_k - v_{n,k}\sin\varphi_k\\ v_{t,k}\\ v_{r,k}\sin\varphi_k + v_{n,k}\cos\varphi_k\end{bmatrix}^T\begin{bmatrix}\hat{x}_k\\ \hat{y}_k\\ \hat{z}_k\end{bmatrix} \tag{13}$$

Then, the locally flat variables (x, y, z, v_x, v_y, v_z) are introduced, with values at t_k corresponding to the components of $\underrightarrow{\mathbf{r}}_k$ and $\underrightarrow{\mathbf{v}}_k$ along $(\hat{x}_k, \hat{y}_k, \hat{z}_k)$, i.e.

$$x_k = r_k\cos\varphi_k \quad y_k = 0 \quad z_k = r_k\sin\varphi_k \tag{14}$$

$$\begin{aligned} v_{x,k} &= v_{r,k}\cos\varphi_k - v_{n,k}\sin\varphi_k\\ v_{y,k} &= v_{t,k}\\ v_{z,k} &= v_{r,k}\sin\varphi_k + v_{n,k}\cos\varphi_k\end{aligned} \tag{15}$$

The locally flat variables are governed by the following equations of motion [36]:

$$\dot{x} = v_x \quad \dot{y} = v_y \quad \dot{z} = v_z \tag{16}$$

$$\begin{aligned} \dot{v}_x &= \widetilde{a}_T\sin\theta_1\cos\theta_2 - g\\ \dot{v}_y &= \widetilde{a}_T\cos\theta_1\cos\theta_2\\ \dot{v}_z &= \widetilde{a}_T\sin\theta_2\end{aligned} \tag{17}$$

where angles (θ_1, θ_2) identify the thrust direction in $(\hat{x}_k, \hat{y}_k, \hat{z}_k)$, g denotes the (local) gravitational acceleration, and $\widetilde{a}_T$ is the thrust acceleration. Angles (θ_1, θ_2) are defined in the following intervals $-\pi < \theta_1 \le \pi$ and $-\pi/2 < \theta_2 \le \pi/2$. When locally flat coordinates are used, thrust acceleration is denoted with symbol $\widetilde{a}_T$ instead of a_T $(= n_T/x_7)$, because the thrust acceleration is assumed constant, to simplify the subsequent analytical developments. Using (x, y, z, v_x, v_y, v_z), the desired conditions at the end of phase 1 are

$$x_f = R_M + h_i \quad z_f = 0 \quad v_{x,f} = 0 \quad v_{y,f} = \omega_M R_M \quad v_{z,f} = 0 \tag{18}$$

where ω_M and R_M denote resepcively the lunar rotation rate and radius. The final condition on $v_{y,f}$ considers the modest inertial velocity of a point on the lunar surface (at equator).

It is worth remarking that these projected variables are used only in the context of the guidance algorithm, and allow a sufficiently accurate approximate description of the spacecraft trajectory, provided that the time of flight is short. In the scientific literature, alternative sets of variables were used for spacecraft reentry problems, leading to different governing equations for the vehicle trajectory. In particular, Mease et al. [37] addressed atmospheric entry using spherical coordinates, while adopting the great arc approximation to obtain the time evolution of a subset of state variables. Instead, Arslantaş et al. [38] employed trajectory governing equations projected onto an inertial frame, and used three Cartesian components to define the spacecraft position, in the context of a lunar descent problem. These two different coordinate sets do not require an iterative projection of variables, unlike locally flat coordinates, introduced in this subsection. Nevertheless, the latter variables allow expressing the related governing equations in the form of Eqs. (16) and (17), and this circumstance plays a crucial role for the iterative (closed-form) solution of the optimal control problem addressed in the next subsection.

3.2. Optimal control

In general, the numerical solution of spacecraft trajectory optimization problems is an offline task, which cannot be achieved using onboard guidance algorithms. In this study, the projected variables, in conjunction with the related governing equations (16) and (17) and boundary conditions (18), are employed for the purpose of identifying the optimal thrust direction that minimizes the time of flight. Let $\mathbf{x} = [x \quad y \quad z \quad v_x \quad v_y \quad v_z]^T$ and $\mathbf{u} = [\theta_1 \quad \theta_2]^T$ represent respectively the state and control vector. The following optimal control problem is introduced:

$$\mathbf{u}^*(t) = \underset{\mathbf{u}}{\operatorname{argmin}} t_f \tag{19}$$

subject to Eqs. (16)-(18),where the star denotes the optimal value of the related vector.

The problem at hand admits an analytical solution that depends on

the initial values of the adjoint vector conjugate to the state equations (16) and (17), if $\widetilde{a}_T$ and g are assumed constant in Eq. (17). To prove this, a Hamiltonian H and the auxiliary function Φ are introduced,

$$H = \lambda_1 v_x + \lambda_2 v_y + \lambda_3 v_z + \lambda_4(\widetilde{a}_T \cos\theta_2 \sin\theta_1 - g) + \lambda_5 \widetilde{a}_T \cos\theta_2 \cos\theta_1 + \lambda_6 \widetilde{a}_T \sin\theta_2 \tag{20}$$

$$\Phi = t_f + \upsilon_1\left[x_f - (R_M + h_i)\right] + \upsilon_2 z_f + \upsilon_3 v_{x,f} + \upsilon_4\left(v_{y,f} - \omega_M R_M\right) + \upsilon_5 v_{z,f} \tag{21}$$

where $\{\lambda_j\}_{j=1,\ldots,6}$ and $\{\upsilon_j\}_{j=1,\ldots,5}$ are respectvely the adjoint variables conjugate to the state equations (16) and (17) and to the boundary conditions (18). The necessary conditions for optimality include the boundary conditions for the adjoint variables [39],

$$\begin{array}{lll} \lambda_{1,f} = \upsilon_1 & \lambda_{2,f} = 0 & \lambda_{3,f} = \upsilon_2 \\ \lambda_{4,f} = \upsilon_3 & \lambda_{5,f} = \upsilon_4 & \lambda_{6,f} = \upsilon_5 \end{array} \tag{22}$$

accompanied by the adjoint equations

$$\dot{\lambda}_1 = -\frac{\partial H}{\partial x} = 0 \Rightarrow \lambda_1 = \lambda_{1,0} \tag{23}$$

$$\dot{\lambda}_2 = -\frac{\partial H}{\partial y} = 0 \Rightarrow \lambda_2 = \lambda_{2,0} = \lambda_{2,f} = 0 \tag{24}$$

$$\dot{\lambda}_3 = -\frac{\partial H}{\partial z} = 0 \Rightarrow \lambda_3 = \lambda_{3,0} \tag{25}$$

$$\dot{\lambda}_4 = -\frac{\partial H}{\partial v_x} = -\lambda_1 \Rightarrow \lambda_4 = \lambda_{4,0} - \lambda_{1,0} t \tag{26}$$

$$\dot{\lambda}_5 = -\frac{\partial H}{\partial v_y} = -\lambda_2 \Rightarrow \lambda_5 = \lambda_{5,0} - \lambda_{2,0} t = \lambda_{5,0} \tag{27}$$

$$\dot{\lambda}_6 = -\frac{\partial H}{\partial v_z} = -\lambda_3 \Rightarrow \lambda_6 = \lambda_{6,0} - \lambda_{3,0} t \tag{28}$$

where subscript 0 denotes the value of the corresponding variable at the initial time t_0. The Pontryagin minimum principle leads to expressing the control angles in terms of the adjoint variables,

$$\mathbf{u}^* = \underset{\mathbf{u}}{\operatorname{argmin}} H \Rightarrow \begin{cases} \sin\theta_1 = -\dfrac{\lambda_4}{\sqrt{\lambda_4^2 + \lambda_5^2}} \quad \cos\theta_1 = -\dfrac{\lambda_5}{\sqrt{\lambda_4^2 + \lambda_5^2}} \\ \theta_2 = -\arcsin\dfrac{\lambda_6}{\sqrt{\lambda_4^2 + \lambda_5^2 + \lambda_6^2}} \end{cases} \tag{29}$$

The condition $\lambda_{5,0} = 0$ leads to $\theta_1 = \pm\pi/2$, which implies violation of the final conditions, therefore $\lambda_{5,0} \neq 0$. Hence, the closed-form expressions of $\{\lambda_1, \lambda_3, \lambda_4, \lambda_5, \lambda_6\}$ can be scaled by $\lambda_{5,0}$, to yield

$$\sin\theta_1 = -\frac{\widetilde{\lambda}_{4,0} - \widetilde{\lambda}_{1,0} t}{\sqrt{\left[\widetilde{\lambda}_{4,0} - \widetilde{\lambda}_{1,0} t\right]^2 + 1}} \quad \cos\theta_1 = \mp\frac{1}{\sqrt{\left[\widetilde{\lambda}_{4,0} - \widetilde{\lambda}_{1,0} t\right]^2 + 1}} \tag{30}$$

$$\theta_2 = -\arcsin\frac{\widetilde{\lambda}_{6,0} - \widetilde{\lambda}_{3,0} t}{\sqrt{\left[\widetilde{\lambda}_{4,0} - \widetilde{\lambda}_{1,0} t\right]^2 + 1 + \left[\widetilde{\lambda}_{6,0} - \widetilde{\lambda}_{3,0} t\right]^2}} \tag{31}$$

where $\widetilde{\lambda}_{j,0} = \lambda_{j,0}/\lambda_{5,0}$ $(j = 1, 3, 4, 6)$. These quantities are collected in $\lambda_0 := [\widetilde{\lambda}_{1,0} \quad \widetilde{\lambda}_{3,0} \quad \widetilde{\lambda}_{4,0} \quad \widetilde{\lambda}_{6,0}]^T$. In Eq. (30), the choice between + and − is related to the sign of $\lambda_{5,0}$, i.e. + is to be selected if $\lambda_{5,0} < 0$, whereas − is chosen if $\lambda_{5,0} > 0$. However, at the initial time the thrust direction must certainly reduce component v_y of the spacecraft velocity, and this means that $\widetilde{a}_T \cos\theta_1 \cos\theta_2 < 0$ (cf. Eq. (17)), i.e. at the initial time $\cos\theta_1 < 0$ (because $-\pi/2 < \theta_2 \leq \pi/2$). Hence, in the second relation of Eq. (30) the sign − is chosen. The analytical expressions (30)–(31) are used in Eqs. (16) and (17) and lead to obtaining closed-form solutions for all of the state variables,

$$\begin{array}{l} x = f_1(\boldsymbol{\lambda}_0, t),\ y = f_2(\boldsymbol{\lambda}_0, t),\ z = f_3(\boldsymbol{\lambda}_0, t) \\ v_x = f_4(\boldsymbol{\lambda}_0, t),\ v_y = f_5(\boldsymbol{\lambda}_0, t),\ v_z = f_6(\boldsymbol{\lambda}_0, t) \end{array} \tag{32}$$

where $\{f_j\}_{j=1,\ldots,6}$ are nonlinear functions of $(\boldsymbol{\lambda}_0, t)$. The explicit expressions for $\{f_j\}_{j=1,\ldots,6}$, written in terms of elementary functions, are reported in Appendix. The preceding solutions for $\{x, z, v_x, v_y, v_z\}$ are evaluated at t_f and inserted in the boundary conditions (18),

$$\begin{array}{l} f_1(\boldsymbol{\lambda}_0, t_f) - (R_M + h_i) = 0,\ f_3(\boldsymbol{\lambda}_0, t_f) = 0,\ f_4(\boldsymbol{\lambda}_0, t_f) = 0 \\ f_5(\boldsymbol{\lambda}_0, t) - \omega_M R_M = 0,\ f_6(\boldsymbol{\lambda}_0, t_f) = 0 \end{array} \tag{33}$$

Equation (33) contains a system of 5 nonlinear equations in 5 unknowns, i.e. t_f and the 4 components of $\boldsymbol{\lambda}_0$. Numerical solvers (such as the embedded routine fsolve in Matlab) can be employed to find the numerical solution of this system in extremely short times (of order of 0.01 s), provided that a proper guess is supplied. To do this, the analysis described in Ref. [36] can be used. In fact, for planar trajectories, corresponding to $z = 0$ and $v_z = 0$, a suitable first-attempt solution is proven to be [36]

$$\begin{array}{l} t_f = \dfrac{v_{y,f} - v_{y,0}}{\widetilde{a}_T} \dfrac{\tan\theta_{1,0}^{(G)} - \tan\theta_{1,f}^{(G)}}{\operatorname{asinh}\left(\tan\theta_{1,f}^{(G)}\right) - \operatorname{asinh}\left(\tan\theta_{1,0}^{(G)}\right)} \\ \widetilde{\lambda}_{1,0}^{(G)} = \dfrac{\tan\theta_{1,0}^{(G)} - \tan\theta_{1,f}^{(G)}}{t_f} \quad \widetilde{\lambda}_{4,0}^{(G)} = \tan\theta_{1,0}^{(G)} \end{array} \tag{34}$$

where $\theta_{1,0}^{(G)}$ and $\theta_{1,f}^{(G)}$ are two guess values for the thrust angle θ_1 at t_0 and t_f, respectively; in this work, $\theta_{1,0}^{(G)} = 180$ deg and $\theta_{1,f}^{(G)} = 120$ deg. The first value corresponds to thrust direction pointing against the instantaneous velocity (at t_0). The second value is such that $\cos\theta_{1,f}^{(G)} = -1/2$, i.e. the thrust component aimed at reducing v_y is assumed to reduce to half of the thrust magnitude at the beginning of phase 1. The remaining two guess values, for $\widetilde{\lambda}_{3,0}^{(G)}$ and $\widetilde{\lambda}_{6,0}^{(G)}$, are both set to 0.

The guidance algorithm repeats the preceding solution process at each sampling time t_k, which becomes the initial time t_0 of the optimal control problem. The final time t_f can be regarded as the time-to-go, and will be denoted with t_{go} hence forward. However, constant values of g and $\widetilde{a}_T$ are needed in each guidance interval, which has duration Δt_S. For the gravitational acceleration, the initial value is chosen, i.e. $g = \mu/r_k^2$. Instead, for the thrust acceleration, the average value of $\widetilde{a}_T$ in $[t_k, t_{k+1}]$ is employed. Let n_k denote the thrust acceleration at t_k; in $[t_k, t_{k+1}]$ the thrust acceleration equals $n_k c/[c - n_k(t - t_k)]$. Hence, $\widetilde{a}_T$ is set to

$$\widetilde{a}_T = \frac{1}{\Delta t_S}\int_{t_k}^{t_{k+1}} \frac{n_k c}{c - n_k(t - t_k)} dt = -\frac{c}{\Delta t_S}\ln\left(1 - \frac{n_k}{c}\Delta t_S\right) \tag{35}$$

It is worth noticing that Eq. (29) resembles the linear tangent steering law [40–42]. However, preceding formulations of this well-consolidated guidance technique introduce approximate assumptions [40] or employ complicated geometric analyses [40] to solve the problem. Instead, the three-dimensional guidance approach proposed in this work is based on the real-time numerical solution of the minimum-time problem formulated in flat coordinates, through enforcement of all the necessary conditions of optimality and without any further approximation or arbitrary assumption on the initial thrust angles θ_1 and θ_2.

3.3. Commanded attitude

The real-time numerical solution of the preceding optimal control problem provides the thrust angles (θ_1, θ_2), which identify the desired

thrust direction in $(\hat{x}_k, \hat{y}_k, \hat{z}_k)$. The latter sequence is obtained from $(\hat{c}_1, \hat{c}_2, \hat{c}_3)$ through a single counterclockwise elementary rotation about axis 3 b y angle ξ_k. Therefore, the commanded thrust direction $\hat{T}^{(C)}$ is given by

$$\begin{aligned}\hat{T}^{(C)} &= [\cos\theta_2 \sin\theta_1 \quad \cos\theta_2 \cos\theta_1 \quad \sin\theta_2][\hat{x}_k \quad \hat{y}_k \quad \hat{z}_k]^T \\ &= [\cos\theta_2 \sin\theta_1 \quad \cos\theta_2 \cos\theta_1 \quad \sin\theta_2]\mathbf{R}_3(\xi_k)[\hat{c}_1 \quad \hat{c}_2 \quad \hat{c}_3]^T \end{aligned} \tag{36}$$

Under the assumption that the thrust is aligned with the spacecraft longitudinal axis, unit vector $\hat{T}^{(C)}$ identifies the commanded direction $\hat{\imath}^{(C)}$. The actual body axis $\hat{\imath}$ must be driven toward $\hat{\imath}^{(C)}$ by the attitude control system. The remaining two commanded body axes, $\hat{j}^{(C)}$ and $\hat{k}^{(C)}$, are defined as

$$\hat{k}^{(C)} := \frac{\hat{c}_3 \times \hat{\imath}^{(C)}}{|\hat{c}_3 \times \hat{\imath}^{(C)}|} \quad \text{and} \quad \hat{j}^{(C)} := \hat{k}^{(C)} \times \hat{\imath}^{(C)} \tag{37}$$

These three unit vectors form vectrix $\underline{\underline{C}}$, i.e. $\underline{\underline{C}} := [\hat{\imath}^{(C)} \quad \hat{j}^{(C)} \quad \hat{k}^{(C)}]$. Because closed-form expressions are available for (θ_1, θ_2), the components of $\hat{\imath}^{(C)}$ (cf. Eq. (36)), $\hat{j}^{(C)}$, and $\hat{k}^{(C)}$ can be written in closed form, as well as the rotation matrix that relates $\underline{\underline{C}}$ to $\underline{\underline{N}}$, i.e. $\underset{C\leftarrow N}{\mathbf{R}}$ defined by $\underline{\underline{N}} = \underline{\underline{C}}\,\underset{C\leftarrow N}{\mathbf{R}}$. Using the kinematics equation that governs the time evolution of rotation matrices, it is straightforward to obtain the commanded angular velocity. In fact,

$$\dot{\underset{C\leftarrow N}{\mathbf{R}}} = -\tilde{\boldsymbol{\omega}}_C \underset{C\leftarrow N}{\mathbf{R}} \Rightarrow \tilde{\boldsymbol{\omega}}_C = -\dot{\underset{C\leftarrow N}{\mathbf{R}}}\,\underset{C\leftarrow N}{\mathbf{R}}^T \tag{38}$$

Because analytical expressions are available for both $\underset{C\leftarrow N}{\mathbf{R}}$ and $\dot{\underset{C\leftarrow N}{\mathbf{R}}}$, matrix $\tilde{\boldsymbol{\omega}}_C$ contains the closed-form expressions of the three components of the commanded angular rate $\overset{N}{\underset{\omega}{\rightarrow}}{}^{C}\left(=\underline{\underline{C}}\boldsymbol{\omega}_C\right)$ along $(\hat{\imath}^{(C)}, \hat{j}^{(C)}, \hat{k}^{(C)})$. The time derivative of $\boldsymbol{\omega}_C$ supplies $\dot{\boldsymbol{\omega}}_C$, which is necessary for nonlinear attitude control (cf. Section 5). However, the preceding relations are used to identify only components $\omega_{C,2}$ and $\omega_{C,3}$ of $\boldsymbol{\omega}_C$. Instead, component $\omega_{C,1}$ (as well as its time derivative) is set to 0, because the existence of a component of the angular velocity along axis 1 is irrelevant for the purpose of correcting the thrust alignment, and is even undesired at touchdown.

3.4. Guidance algorithm

The guidance algorithm is intended to provide the commanded orientation and angular rate to the attitude control system. Therefore, the guidance algorithm has

$$\begin{aligned}&\text{Input}: r_k, \xi_k, \varphi_k, v_{r,k}, v_{t,k}, v_{n,k}, n_k \ (\text{at } t_k) \rightarrow \\ &\text{Output}: t_{go} \text{ and } \underset{C\leftarrow N}{\mathbf{R}}, \boldsymbol{\omega}_C, \dot{\boldsymbol{\omega}}_C \ (\text{in } [t_k, t_{k+1}])\end{aligned} \tag{39}$$

In summary, the following steps are completed at each sampling time t_k:

(1) the spherical coordinates are converted into locally flat variables (cf. Eqs. (12) and (13)),
(2) the guess solution for the optimal control problem is identified (cf. Eq. (34)),
(3) the equation system (33) is solved numerically, and
(4) t_{go} and the closed-form expressions for θ_1, θ_2, $\underset{C\leftarrow N}{\mathbf{R}}$, $\boldsymbol{\omega}_C$, and $\dot{\boldsymbol{\omega}}_C$ in $[t_k, t_{k+1}]$ are obtained.

The last guidance interval occurs when $t_{go} \le \Delta t_S$.

It is worth stressing that the guidance approach at hand requires no interpolation or finite-difference method for finding $\dot{\underset{C\leftarrow N}{\mathbf{R}}}$ and $\dot{\boldsymbol{\omega}}_C$, thanks to the availability of analytical expressions for the previously mentioned variables.

4. Phase 2. predictive bang-off-bang guidance

Phase 2 starts at the end of arc 1, and is aimed at reaching the lunar surface with modest vertical velocity, zero horizontal velocity and angular rate. The threshold (lower) value for v_r, denoted with $v_{r,th}$, is set to -1 m/s. This means that the radial velocity at touchdown is constrained the interval $[-1, 0[$ m/s. Instead, the horizontal velocity magnitude at touchdown must not exceed 0.1 m/s (and this maximum value is denoted with $v_{hor}^{(max)}$, i.e. $v_{hor}^{(max)} = 0.1$ m/sec). The main thruster is responsible for decelerating the spacecraft. However, especially at the very beginning of phase 2, the spacecraft has incorrect alignment, therefore it is convenient to use the main thruster for reducing the horizontal velocity relative to the (rotating) lunar surface, given by $\left(\underset{\rightarrow}{\mathbf{v}} - \omega_M R_M \hat{t}\right)$. Thus, the main thruster is ignited only if $\hat{\imath}\cdot\left(\underset{\rightarrow}{\mathbf{v}} - \omega_M R_M \hat{t}\right) < 0$. Instead, the side jets are used mainly for attitude maneuvering. Yet, when the correct alignment is attained, they can be ignited in pairs (on the same side of the descent vehicle, in continuous mode), to reduce the relative horizontal velocity. Vertical alignment is described by $r_{11} := \cos(\hat{\imath}\cdot\hat{r})$, and two threshold values for r_{11} are introduced: (a) $r_{11}^{(L)}$, set to 0.9, and (b) $r_{11}^{(U)}$, set to 0.999. Three cases can occur: (i) $r_{11} < r_{11}^{(L)}$, (ii) $r_{11}^{(L)} \le r_{11} \le r_{11}^{(U)}$, and (iii) $r_{11} > r_{11}^{(U)}$. In case (i), the side jets are used for attitude maneuvering only. In case (ii), correct alignment is close but not yet reached, and the side jets are used both for horizontal velocity correction and for attitude corrections. In case (iii), correct alignment is reached to a satisfactory accuracy, and the side jets are used for trajectory corrections only, i.e. to reduce the horizontal velocity, if the latter exceeds the limiting value $v_{hor}^{(max)}$.

The following steps, repeated iteratively at each sampling time t_k, form the predictive bang-off-bang guidance scheme, aimed at identifying the ignition times for both the main thruster and the side jets:

(1) evaluate the expected radial velocity at t_{k+1}, $v_{r,k+1}^{(E)}$, assuming vertical descent and no propulsion in $[t_k, t_{k+1}]$;
(2) evaluate the expected radial velocity at touchdown, $v_{r,f}^{(E)}$, assuming vertical descent from time t_{k+1} and thrust always on and directed vertically; if touchdown does not occur and the altitude starts increasing, set $v_{r,f}^{(E)}$ to infinity;
(3) evaluate r_{11};
(4) evaluate $\eta_M := \hat{\imath}_k \cdot \left(\underset{\rightarrow}{\mathbf{v}}_k - \omega_M R_M \hat{t}_k\right)$;
(5) evaluate the horizontal velocity relative to the lunar surface, i.e. $\underset{\rightarrow}{\mathbf{v}}_{hor,k} := \underset{\rightarrow}{\mathbf{v}}_k - \omega_M R_M \hat{t}_k - v_{r,k}\hat{r}_k$;
(6) allocate the side jets (for either attitude maneuvering or horizontal velocity correction):
   a. If $(r_{11} < r_{11}^{(L)})$ or $\left(\left|\underset{\rightarrow}{\mathbf{v}}_{hor,k}\right| < v_{hor}^{(max)}\right)$, then ignite the side jets for attitude maneuvering;
   b. If $(r_{11} > r_{11}^{(U)})$ and $\left(\left|\underset{\rightarrow}{\mathbf{v}}_{hor,k}\right| > v_{hor}^{(max)}\right)$, then ignite the side jets for horizontal velocity correction;
   c. If $(r_{11}^{(L)} \le r_{11} \le r_{11}^{(U)})$ and $\left(\left|\underset{\rightarrow}{\mathbf{v}}_{hor,k}\right| > v_{hor}^{(max)}\right)$, then allocate a fraction of the sampling time interval to attitude maneuvering, and the rest to horizontal velocity correction; the lengths of the two partitions of the sampling time interval depend on r_{11};
   d. If $(r_{11} > r_{11}^{(U)})$ and $\left(\left|\underset{\rightarrow}{\mathbf{v}}_{hor,k}\right| \le v_{hor}^{(max)}\right)$, then switch off the side jets;

(7) define the ignition of the main engine in $[t_k, t_{k+1}]$, on the basis of a hysteretic scheme:

a. If (thrust was off in $[t_{k-1}, t_k]$ and $v_{r,th} \le v_{r,f}^{(E)} \le 0$) or (($r_{11} < r_{11}^{(L)}$) and ($\eta_M \ge 0$)), then the main engine is off in $[t_k, t_{k+1}]$;

b. If (thrust was on in $[t_{k-1}, t_k]$ and $v_{r,th} \le v_{r,f}^{(E)} \le 0$) or (($r_{11} < r_{11}^{(L)}$) and ($\eta_M < 0$)), then the main engine is on in $[t_k, t_{k+1}]$;

c. If ($v_{r,f}^{(E)} < v_{r,th}$) and ($r_{11} \ge r_{11}^{(L)}$), then the main engine is on in $[t_k, t_{k+1}]$;

d. If ($v_{r,f}^{(E)} > 0$) and ($r_{11} < r_{11}^{(L)}$), then the main engine is off in $[t_k, t_{k+1}]$.

The previous conditions in steps (6) and (7) are checked sequentially, e.g. if condition (7 b) is fulfilled, then the main engine is ignited in $[t_k, t_{k+1}]$, and conditions (7c) and (7 d) need not to be checked. To clarify the possible outcomes of step (7), Table 1 reports all the possible combinations of conditions, with the related outcome in the last column, i.e. either ignition or shutdown of the main engine. The preceding scheme yields a bang-off-bang sequence of ignitions for the main thruster and the side jets. When the latter are employed for attitude maneuvering, the attitude control algorithm, in conjunction with pulse modulation, identifies the actual ignition times in the time interval $[t_k, t_{k+1}]$. Moreover, the desired pointing direction of the longitudinal axis of the spacecraft is aligned with $\hat{r}_k$, and this identifies the commanded single-axis attitude.

5. Quaternion-based nonlinear reduced-attitude control

The guidance algorithm provides the desired orientation and angular rates, which must be pursued by the attitude control system. However, only the alignment of the longitudinal axis $\hat{\imath}$ with $\hat{\imath}^{(C)}$ is crucial for the purpose of pointing the thrust toward the correct direction. A reduced-attitude-tracking algorithm, which aims at pursuing the desired alignment for a single axis, represents a suitable solution to the problem of interest. This section addresses a new feedback quaternion-based reduced-attitude-tracking algorithm.

5.1. Relative attitude kinematics

As a preliminary step, the commanded Euler parameters (quaternions) are obtained from $\underset{C\leftarrow N}{\mathbf{R}}$ and denoted with $\{q_0^{(C)}, \mathbf{q}^{(C)}\}$. The actual body axes are aligned with the unit vectors that form $\underline{\underline{B}}$. The rotation matrix that relates $\underline{\underline{B}}$ and $\underline{\underline{C}}$, associated with the commanded body axes, can be written in terms of the error quaternion $\{q_0^{(E)}, \mathbf{q}^{(E)}\}$ [34],

$$\underset{B\leftarrow C}{\mathbf{R}} = \underset{B\leftarrow NC\leftarrow N}{\mathbf{R}}\,\underset{B\leftarrow N}{\mathbf{R}}^{T} = \left\{\left[q_0^{(E)}\right]^2 - \left[\mathbf{q}^{(E)}\right]^T\mathbf{q}^{(E)}\right\}\mathbf{I}_{3\times 3} + 2\mathbf{q}^{(E)}\left[\mathbf{q}^{(E)}\right]^T - 2q_0^{(E)}\tilde{\mathbf{q}}^{(E)} \tag{40}$$

The first row of matrix $\underset{B\leftarrow C}{\mathbf{R}}$ contains the components of axis $\hat{\imath}$ in $\underline{\underline{C}}$ and is given by

$$\begin{bmatrix} \left[q_0^{(E)}\right]^2 + \left[q_1^{(E)}\right]^2 - \left[q_2^{(E)}\right]^2 - \left[q_3^{(E)}\right]^2 \\ 2\left[q_1^{(E)}q_2^{(E)} + q_0^{(E)}q_3^{(E)}\right] \\ 2\left[q_1^{(E)}q_3^{(E)} - q_0^{(E)}q_2^{(E)}\right] \end{bmatrix}^T \tag{41}$$

where subscripts 1, 2, and 3 refer to the components of $\mathbf{q}^{(E)}$. It is apparent that correct alignment of $\hat{\imath}$ and $\hat{\imath}^{(C)}$, i.e. $\hat{\imath} \equiv \hat{\imath}^{(C)}$, corresponds to

$$\left[q_2^{(E)}\right]^2 + \left[q_3^{(E)}\right]^2 = 0 \tag{42}$$

Moreover, the kinematics equations for $\{q_0^{(E)}, \mathbf{q}^{(E)}\}$ are [43]

$$\dot{q}_0^{(E)} = -\frac{1}{2}\left[\mathbf{q}^{(E)}\right]^T\boldsymbol{\omega}_E \tag{43}$$

$$\dot{\mathbf{q}}^{(E)} = \frac{1}{2}\left[q_0^{(E)}\mathbf{I}_{3\times 3} + \tilde{\mathbf{q}}^{(E)}\right]\boldsymbol{\omega}_E \tag{44}$$

where $\boldsymbol{\omega}_E := \boldsymbol{\omega} - \underset{B\leftarrow C}{\mathbf{R}}\,\boldsymbol{\omega}_C$. The time evolution of the rotation matrix $\underset{B\leftarrow C}{\mathbf{R}}$ is governed by the following equation [43]:

$$\dot{\underset{B\leftarrow C}{\mathbf{R}}} = -\tilde{\boldsymbol{\omega}}_E\,\underset{B\leftarrow C}{\mathbf{R}} \tag{45}$$

5.2. Feedback control law and stability analysis

The target set for the attitude tracking problem is

$$\left[q_2^{(E)}\right]^2 + \left[q_3^{(E)}\right]^2 = 0 \quad \text{and } \boldsymbol{\omega}_E = \mathbf{0} \tag{46}$$

and corresponds to achieving $\boldsymbol{\omega}_E = \mathbf{0}$ and the correct alignment of axis 1, while the commanded orientation of the remaining two axes is not tracked.

Proposition 1. For the torque vector $\mathbf{T}_C$, the following feedback control law is introduced:

$$\mathbf{T}_C = \tilde{\boldsymbol{\omega}}\mathbf{J}_C^{(B)}\boldsymbol{\omega} + \dot{\mathbf{J}}_C^{(B)}\boldsymbol{\omega} + \mathbf{J}_C^{(B)}\left[\underset{B\leftarrow C}{\mathbf{R}}\,\dot{\boldsymbol{\omega}}_C - \tilde{\boldsymbol{\omega}}_E\,\underset{B\leftarrow C}{\mathbf{R}}\,\boldsymbol{\omega}_C\right] - \mathbf{J}_C^{(B)}\mathbf{A}^{-1}\left[\mathbf{B}\boldsymbol{\omega}_E + \mathbf{f}\left(q_0^{(E)}, \mathbf{q}^{(E)}\right)\right] \tag{47}$$

where

$$\mathbf{f}\left(q_0^{(E)}, \mathbf{q}^{(E)}\right) := \begin{bmatrix} 0 \\ q_0^{(E)}q_2^{(E)} + q_1^{(E)}q_3^{(E)} \\ q_0^{(E)}q_3^{(E)} - q_1^{(E)}q_2^{(E)} \end{bmatrix}^T \tag{48}$$

and **A** and **B** are two constant positive definite matrices; A is also symmetric. The control law (47) drives the dynamical system described by Eqs. (11) and (43)-(44) toward the invariant set composed of

(1) $\boldsymbol{\omega}_E = \mathbf{0}$ and $[q_2^{(E)}]^2 + [q_3^{(E)}]^2 = 0$

(2) $\boldsymbol{\omega}_E = \mathbf{0}$ and $[q_1^{(E)}]^2 + [q_0^{(E)}]^2 = 0$

Table 1
Decision table for ignition of the main engine.

$v_{r,f}^{(E)}$	r_{11}	η_M	Thrust in $[t_{k-1}, t_k]$	Thrust in $[t_k, t_{k+1}]$
$v_{r,f}^{(E)} < v_{r,th}$	$< r_{11}^{(L)}$	≥ 0	ON or OFF	OFF (7a)
$v_{r,f}^{(E)} < v_{r,th}$	$< r_{11}^{(L)}$	< 0	ON or OFF	ON (7 b)
$v_{r,f}^{(E)} < v_{r,th}$	$\ge r_{11}^{(L)}$	≥ 0	ON or OFF	ON (7c)
$v_{r,f}^{(E)} < v_{r,th}$	$\ge r_{11}^{(L)}$	< 0	ON or OFF	ON (7c)
$v_{r,th} \le v_{r,f}^{(E)} \le 0$	$< r_{11}^{(L)}$	≥ 0	ON or OFF	OFF (7a)
$v_{r,th} \le v_{r,f}^{(E)} \le 0$	$< r_{11}^{(L)}$	< 0	ON or OFF	ON (7 b)
$v_{r,th} \le v_{r,f}^{(E)} \le 0$	$\ge r_{11}^{(L)}$	≥ 0	OFF	OFF (7a)
$v_{r,th} \le v_{r,f}^{(E)} \le 0$	$\ge r_{11}^{(L)}$	≥ 0	ON	ON (7 b)
$v_{r,th} \le v_{r,f}^{(E)} \le 0$	$\ge r_{11}^{(L)}$	< 0	OFF	OFF (7a)
$v_{r,th} \le v_{r,f}^{(E)} \le 0$	$\ge r_{11}^{(L)}$	< 0	ON	ON (7 b)
$v_{r,f}^{(E)} > 0$	$< r_{11}^{(L)}$	≥ 0	ON or OFF	OFF (7a)
$v_{r,f}^{(E)} > 0$	$< r_{11}^{(L)}$	< 0	ON or OFF	ON (7 b)
$v_{r,f}^{(E)} > 0$	$\ge r_{11}^{(L)}$	≥ 0	ON or OFF	OFF (7 d)
$v_{r,f}^{(E)} > 0$	$\ge r_{11}^{(L)}$	≥ 0	ON or OFF	OFF (7 d)

Proof. As a first step, the following candidate Lyapunov function is introduced:

$$V = \frac{1}{2}\boldsymbol{\omega}_E^T \mathbf{A}\boldsymbol{\omega}_E + \left[q_2^{(E)}\right]^2 + \left[q_3^{(E)}\right]^2 \tag{49}$$

It is apparent that this function is always positive definite and vanishes only in the target set. Second, V has continuous partial derivatives. Using Eqs. (11), (44) and (45), the time derivative of V equals

$$\dot{V} = \boldsymbol{\omega}_E^T \mathbf{A}\left\{\left[\mathbf{J}_C^{(B)}\right]^{-1}\left(-\tilde{\boldsymbol{\omega}}\mathbf{J}_C^{(B)}\boldsymbol{\omega} - \dot{\mathbf{J}}_C^{(B)}\boldsymbol{\omega} + \mathbf{T}_C\right) - \underset{B\leftarrow C}{\mathbf{R}}\dot{\boldsymbol{\omega}}_C + \tilde{\boldsymbol{\omega}}_E \underset{B\leftarrow C}{\mathbf{R}}\boldsymbol{\omega}_C\right\} + \left[q_0^{(E)}q_2^{(E)} + q_1^{(E)}q_3^{(E)}\right]\omega_{E,2} + \left[q_0^{(E)}q_3^{(E)} - q_1^{(E)}q_2^{(E)}\right]\omega_{E,3} \tag{50}$$

where $\omega_{E,j}$ denotes component j of $\boldsymbol{\omega}_E$. Insertion of the feedback law (47) leads to

$$\dot{V} = -\boldsymbol{\omega}_E^T \mathbf{B}\boldsymbol{\omega}_E \tag{51}$$

which is negative (because **B** is positive definite), except at $\boldsymbol{\omega}_E = \mathbf{0}$, where $\dot{V}$ vanishes. Definitely, V is a positive definite function, with continuous partial derivatives and such that $\dot{V} < 0$ (unless $\boldsymbol{\omega}_E = \mathbf{0}$), therefore V is a Lyapunov function [41].

Moreover, because $\dot{V}$ is continuous and negative (except at $\boldsymbol{\omega}_E = \mathbf{0}$), the condition $V(q_0^{(E)}(t), \mathbf{q}^{(E)}(t), \boldsymbol{\omega}_E(t)) \leq V(q_0^{(E)}(t_0), \mathbf{q}^{(E)}(t_0), \boldsymbol{\omega}_E(t_0))$ defines a compact set C. The invariant set, which plays a crucial role in the LaSalle's principle, is to be sought in $A \cap C$, i.e. in the portion of the attracting set A contained in C. By definition, the invariant set collects all the dynamical states (in the attracting set) that remain unaltered. This means that once the invariant set is reached, $\boldsymbol{\omega}_E = \mathbf{0}$ at future times, which implies $\dot{\boldsymbol{\omega}}_E = \mathbf{0}$, i.e.

$$\dot{\boldsymbol{\omega}}_E = \dot{\boldsymbol{\omega}} - \underset{B\leftarrow C}{\mathbf{R}}\dot{\boldsymbol{\omega}}_C + \tilde{\boldsymbol{\omega}}_E \underset{B\leftarrow C}{\mathbf{R}}\boldsymbol{\omega}_C = \dot{\boldsymbol{\omega}} - \underset{B\leftarrow C}{\mathbf{R}}\dot{\boldsymbol{\omega}}_C = \mathbf{0} \tag{52}$$

Using Eqs. (11) and (47), the preceding relation simplifies to

$$\mathbf{A}^{-1}\mathbf{f}\left(q_0^{(E)}, \mathbf{q}^{(E)}\right) = \mathbf{0} \Rightarrow \mathbf{f}\left(q_0^{(E)}, \mathbf{q}^{(E)}\right) = \mathbf{0} \tag{53}$$

i.e.

$$q_0^{(E)}q_2^{(E)} + q_1^{(E)}q_3^{(E)} = 0 \quad \text{and} \quad q_0^{(E)}q_3^{(E)} - q_1^{(E)}q_2^{(E)} = 0 \tag{54}$$

Let $\left\{\underset{B\leftarrow C}{\mathbf{R}}\right\}_{jk}$ denote element (j, k) of $\underset{B\leftarrow C}{\mathbf{R}}$. Insertion of the two conditions (54) in $\underset{B\leftarrow C}{\mathbf{R}}$, written in terms of the error quaternion (cf. Eq. (40)), leads to obtaining $\left\{\underset{B\leftarrow C}{\mathbf{R}}\right\}_{11} = \pm 1$. Thus, the invariant set includes two subsets:

(S) $\boldsymbol{\omega}_E = \mathbf{0}$ and $\left\{\underset{B\leftarrow C}{\mathbf{R}}\right\}_{11} = 1$ or, equivalently, $\boldsymbol{\omega}_E = \mathbf{0}$ and $\left[q_2^{(E)}\right]^2 + \left[q_3^{(E)}\right]^2 = 0$, and

(U) $\boldsymbol{\omega}_E = \mathbf{0}$ and $\left\{\underset{B\leftarrow C}{\mathbf{R}}\right\}_{11} = -1$ or, equivalently, $\boldsymbol{\omega}_E = \mathbf{0}$ and $\left[q_1^{(E)}\right]^2 + \left[q_0^{(E)}\right]^2 = 0$. □

The preceding proposition identifies the two subsets that form the invariant set. Stability of these two subsets is addressed in the following

Proposition 2. With reference to the dynamical system described by Eqs. (11) and (43)-(44), controlled with the feedback law (47), invariant subset S enjoys asymptotic stability, whereas invariant subset U is unstable.

Proof. Proposition 2 identifies invariant subsets S and U. This means that $\boldsymbol{\omega}_E = \mathbf{0}$ at all future times implies either (a) $\left[q_2^{(E)}\right]^2 + \left[q_3^{(E)}\right]^2 = 0$ or (b) $\left[q_1^{(E)}\right]^2 + \left[q_0^{(E)}\right]^2 = 0$. Violation of both conditions (a) and (b) at a generic time $\bar{t}$ implies $\boldsymbol{\omega}_E \neq \mathbf{0}$ at time $(\bar{t} + \delta t)$, where $\delta t > 0$ is an arbitrary small time. As a result, $\dot{V} = -\boldsymbol{\omega}_E^T \mathbf{B}\boldsymbol{\omega}_E < 0$ if both (a) and (b) are violated.

In subset U, $\dot{V} = 0$ and $V = 1$. At time $\bar{t}$, the following neighborhood of subset U can be identified: $\{\boldsymbol{\omega}_E = \mathbf{0}, \left[q_2^{(E)}\right]^2 + \left[q_3^{(E)}\right]^2 = 1 - \varepsilon\}$, where ε is an arbitrary small, positive constant. In this neighborhood, $V = 1 - \varepsilon < 1$. Moreover, at $(\bar{t} + \delta t)$ (with δt arbitrarily small and positive), $\boldsymbol{\omega}_E \neq \mathbf{0}$ and $\dot{V} = -\boldsymbol{\omega}_E^T \mathbf{B}\boldsymbol{\omega}_E < 0$ as a result. This condition implies that $V < 1$ at all future times, which prevents the dynamical system from converging to $V = 1$, condition associated with subset U. The existence of an unstable neighborhood of subset U proves that invariant subset U is unstable.

In subset S, $\dot{V} = 0$ and $V = 0$ (absolute minimum value of V). At time $\bar{t}$, in a sufficiently small neighborhood of subset S, either condition (a) or equality $\boldsymbol{\omega}_E = \mathbf{0}$ is violated. In both cases, at $(\bar{t} + \delta t)$, $0 < V < 1$ and $\dot{V} < 0$. Monotonic decrease of V drives the dynamical system toward the global minimum of V, which equals 0 and corresponds to subset S. This proves the attractivity of invariant subset S. The Lyapunov theorem [44] for invariant sets ensures the stability of subset S. Attractivity and stability imply asymptotic stability. □

In short, the invariant set includes two subsets, denoted with S and U. It is apparent that subset S is the target set, whereas subset U corresponds to the alignment of body axis 1 toward a direction opposite to the desired one. While subset U represents an unstable set, the target set is asymptocally stable. This circumstance has the remarkable consequence that – from the numerical point of view – the dynamical system of interest can be expected to enjoy global stability at the desired alignment in practical operational conditions, if the feedback law (47) is used.

5.3. Gain selection

The feedback control law (47) is defined in terms of two constant, positive definite matrices, i.e. **A** and **B**. Selection of these matrices affects the transient behavior and the convergence time of the actual attitude toward the commanded one. In this research, these two matrices are selected by assuming that both of them are diagonal and written in terms of two positive constants c_1 and c_2, i.e.

$$\mathbf{A}^{-1} = c_1\mathbf{I}_{3\times 3} \quad \text{and} \quad \mathbf{B} = c_2\mathbf{I}_{3\times 3} \tag{55}$$

For the purpose of preliminary selection of the control gains, in three-axial (full-attitude) maneuvers, the rotation is assumed to occur about the eigenaxis, and the gains of the quaternion-based nonlinear feedback law are found using the second-order equation [43].

$$\ddot{\varphi}_E + c_1c_2\dot{\varphi}_E + c_1 \sin\frac{\varphi_E}{2} = 0 \tag{56}$$

where φ_E is the principal angle. If φ_E is sufficiently small, then $\sin(\varphi_E/2) \approx \varphi_E/2$, and Eq. (56) assumes the form of a second-order linear differential equation,

$$\ddot{\varphi}_E + 2\zeta\omega_n\dot{\varphi}_E + \omega_n^2\varphi_E = 0 \quad \text{with } c_1 = 2\omega_n^2 \text{ and } c_2 = \frac{\zeta}{\omega_n} \tag{57}$$

The associated second-order system has damping coefficient ζ and natural frequency ω_n. Selection of these two parameters, which have a straightforward interpretation in relation to the transient behavior, leads to selecting two proper values of c_1 and c_2. Although the reduced-attitude control algorithm differs to some extent from the full-attitude control scheme, this methodology for preliminary selection of **A** and **B** is adopted and implemented, by setting $\omega_n = 2\ s^{-1}$ and $\zeta = 1$.

5.4. Pulse-modulated actuation using side jets

The control torque defined by Eq. (47) is provided by the attitude control system, composed of the 12 side-jets represented in Fig. 1. These actuators are equally distributed in 3 sets, indicated with subscript i = 1,2,3 and referring to axis $\hat{\imath}$, $\hat{\jmath}$, and $\hat{k}$. For set i, the side jets are actuated in pairs, to provide either a positive or a negative torque component i. As an example, in Fig. 1 ignition of jets 2 and 6 (of set 1) yields a positive torque component along $\hat{\imath}$. The i-th set of actuators yields a torque magntiude $T_{c,i}^{(max)} = 2b_iF_i(t)$, which depends on the thrust $F_i(t)$ of the side jets and their fixed distance b_i with respect to the related body axis. As the magnitude of $F_i(t)$ cannot be controlled, the only option to tune the torque magnitude is operating the side jets in pulse mode, by modulating their ignition time $t_{ON,i}$ over time intervals named duty cycles (DC). The average torque yielded by the modulated actuation over each DC approximately equals the desired torque, with accuracy depending on the modulator design.

The pulse width modulation [28] (PWM) is used to convert the nominal control torque from Eq. (47) into the three time intervals $t_{ON,i}$, one for each torque component. In the PWM the value of DC is constant in each phase (cf. Table 2), therefore the values of $t_{ON,i}$ are calculated at constant time intervals using the following expressions:

$$t_{ON,i} = \begin{cases} DC & \text{if } |T_{c,i}| \geq T_{c,i}^{(max)} \\ \dfrac{|T_{c,i}|}{T_{c,i}^{(max)}} DC & \text{if } T_{c,i}^{(min)} < |T_{c,i}| < T_{c,i}^{(max)} \\ 0 & \text{if } |T_{c,i}| \leq T_{c,i}^{(min)} \end{cases} \tag{58}$$

where DC is a design parameter of the modulator, which must be accurately selected during the design process [29], and $T_{c,i}^{(min)} = T_{c,i}^{(max)} t_{ON}^{(min)}/DC$ is the minimum torque magnitude that can be produced by the side jets associated with set i; $T_{c,i}^{(min)}$ depends on their minimum actuation time $t_{ON}^{(min)}$, therefore it is a technological constraint [30].

The side jets are assumed to be monopropellant thrusters, where the propellant is fed by the action of an inert pressurant gas. The reservoir pressure of the gas decreases in time due to gas ejection, with consequent exponential reduction of the thrust, as specified in Section 2. For the numerical analysis discussed in the following section, all the side jets are assumed to share the same pressurant gas tank and design specifications, reported in Table 2.

6. Numerical simulations

The guidance, control, and actuation architecture proposed in this study is tested in the presence of nonnominal flight conditions, namely errors in (i) the initial components of position and velocity and (ii) initial attitude and angular rate. The sampling time interval is set to 1 s for phase 1 and 0.1 s for phase 2. Several zonal harmonics of the selenopotential are responsible of further deviations from the nominal flight conditions, because the guidance algorithm considers only a piecewise constant gravitational acceleration. A Monte Carlo (MC) campaign, composed of 100 simulations, is run, with the intent of testing the methodology at hand. Initial stochastic Gaussian displacements on the position and velocity variables are assumed, with zero mean and the following standard deviations: $r_0^{(\sigma)} = 2$ km, $\varphi_0^{(\sigma)} = 0.163$ deg (corresponding to 5 km in the direction normal to the orbital plane), and $v_0^{(\sigma)} = 50$ m/s, where $\chi_0^{(\sigma)}$ denotes the initial standard deviation of the generic variable χ; $v_0^{(\sigma)}$ represents the standard deviation on the initial velocity magnitude; the random direction of the velocity displacement has uniform distribution over the two-dimensional sphere. Similarly, errors on the initial attitude angles and rates are introduced. The initial attitude is defined as

$$\underline{\underline{B}}^T(t_0) = \mathbf{R}_1(\Phi)\mathbf{R}_2(\Theta)\mathbf{R}_3(\Psi)\underline{\underline{N}}^T(t_0) \tag{59}$$

where angles Ψ, Θ, and Φ have Gaussian distribution, with standard deviation of 30 deg and mean values $\overline{\Psi}_0 = -90$ deg, $\overline{\Theta}_0 = 0$ deg, and $\overline{\Phi}_0 = 0$ deg. The initial attitude rates have Gaussian distribution as well, zero mean, and standard deviation equal to 10 deg/s. Moreover, the valves are modeled as first-order systems, with time constant set to 3.6 msec [45]. For the purpose of improving the description of the thrusters operational behavior, noise is modeled as well, by assuming the following actual torque $T_{C,real}(t)$, supplied by each pair of side jets:

$$T_{C,real}(t) = T_{C,nom}(t) + r_n(t) \tag{60}$$

where $T_{C,nom}(t)$ is the nominal torque, whereas $r_n(t)$ is a piecewise linear function of time, used to interpolate $r_{n,j}$ $(= r_n(t_j))$ stochastic samples. The latter are equally spaced, with a time resolution of 1 msec, i.e. $t_{j+1} - t_j = 1$ msec. The values $r_{n,j}$ have uniform distribution in the range $[-0.01, 0.01]T_{C,nom,0}$, where $T_{C,nom,0}$ is the nominal torque magnitude at the initial time; $r_{n,j}$ is set to 0 if $T_{C,nom}(t_j) = 0$.

For phase 1, Fig. 3 through 8 portray the time histories of altitude, declination, radial velocity, relative transverse velocity $v_{R,t}$, defined as $v_{R,t} = v_t - \omega_M r \cos\varphi$, normal velocity (all from the MC campaign), and modulated torque (in a single MC run). For phase 2, Fig. 9 through 17 depict the time histories of altitude, velocity and angular velocity components, misalignment angle φ_f between the commanded and the actual longitudinal axis (all from the MC campaign), and modulated torque (in a single MC run). These variables regard the center of mass of the vehicle, whose final altitude equals 0.95 m, and takes into account its actual position inside the descent vehicle. Fig. 18 portrays a zoom on component 3 of the control torque, in the first 2 s of phase 2 (single simulation). Exponential time histories at transitions from ignitions and shutdowns of the side jets are apparent, as well as noise. The statistics on the final values at touchdown regard the velocity components $(v_r, v_{R,t}, v_n)$ for both the center of mass and the four pads that touch the lunar surface, as well as the values of declination, misalignment angle, components of the angular velocity, time of flight, and mass. Tables 3 and 4 report these statistics, which unequivocally testify to the excellent performance of the guidance, control, and actuation architecture at hand. Finally, Table 5 contains the statistics on runtime, on an Intel core i7 @ 1.30 GHz, i.e. its average, maximum, minimum value, and standard

Table 2
Design parameters of the side jets.

Parameter	Symbol	Value	Unit
Initial thrust	$F_i(t_0)$	200	N
Torque arm	b_i	1	m
Time constant	t_{car}	7027	sec
Duty cycle in phase 1	DC	0.2	sec
Duty cycle in phase 2	DC	0.05	sec
Minimum acuation time	$t_{ON}^{(min)}$	0.02	sec

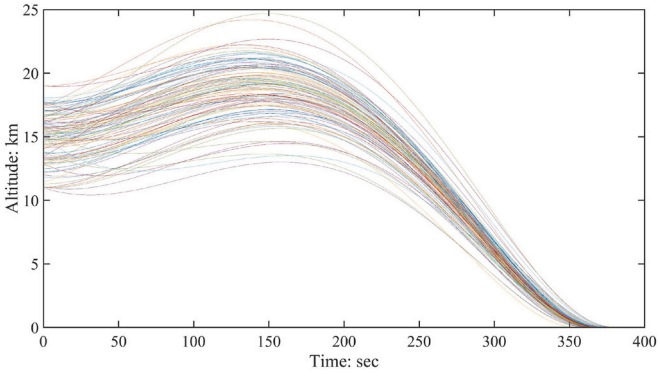

Fig. 3. Phase 1: time histories of altitude (MC campaign).

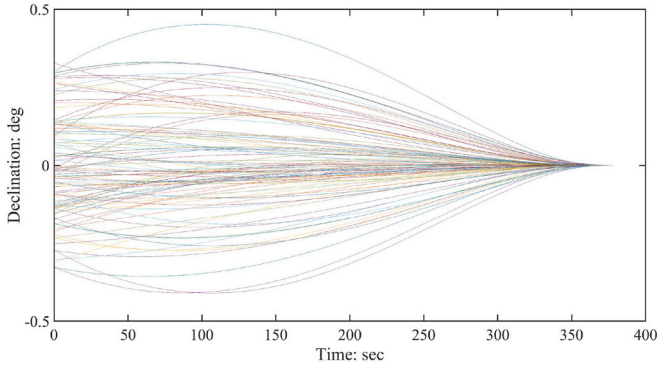

Fig. 4. Phase 1: time histories of declination (MC campaign).

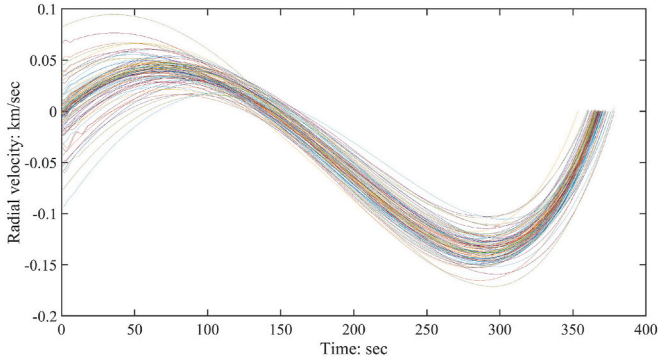

Fig. 5. Phase 1: time histories of the radial velocity (MC campaign).

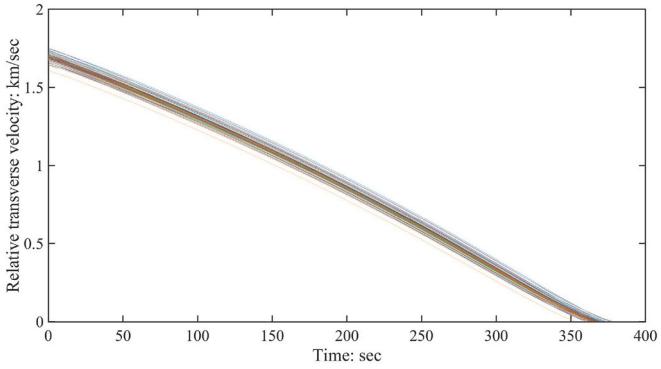

Fig. 6. Phase 1: time histories of the relative transverse velocity (MC campaign).

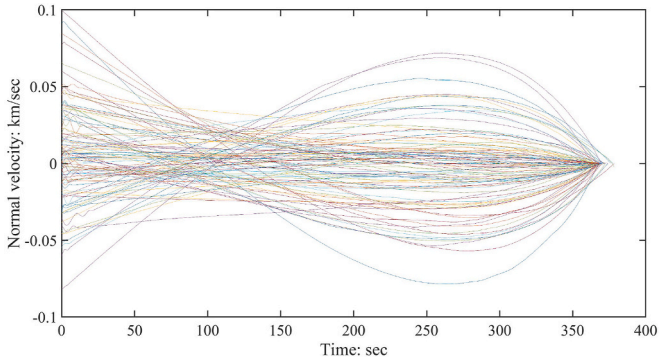

Fig. 7. Phase 1: time histories of the normal velocity (MC campaign).

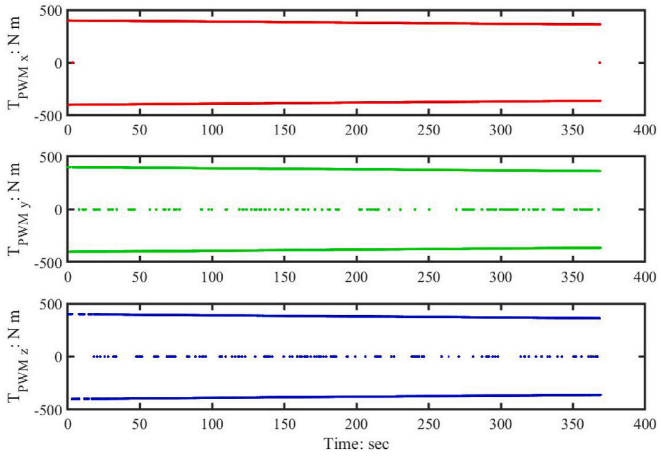

Fig. 8. Phase 1: time histories of the desired torque components yielded by PWM (single MC simulation).

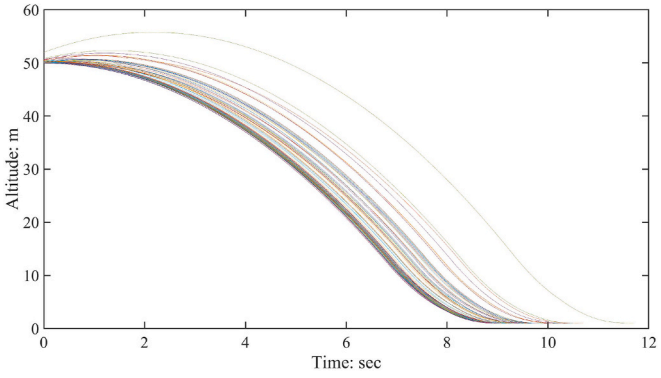

Fig. 9. Phase 2: time histories of altitude (MC campaign).

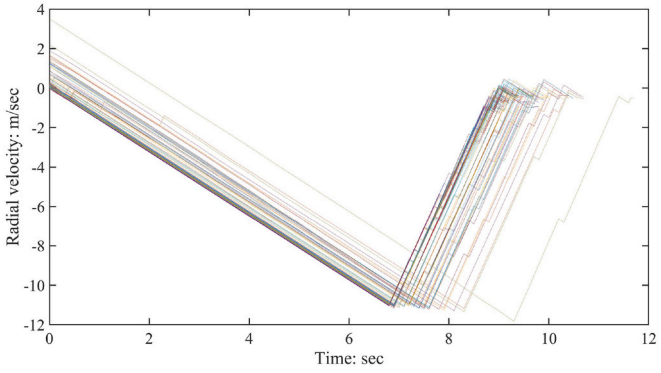

Fig. 10. Phase 2: time histories of the radial velocity (MC campaign).

deviation, obtained from 100 Monte Carlo simulations, in which thrusters noise is omitted. In fact, including the latter increases the runtime, because of the longer time needed for the integration the spacecraft dynamics, whereas the computation of the guidance and control action is substantially unaffected. Consequently, omitting the thrusters noise allows obtaining a more meaningful evaluation of the computational time required by the guidance and control algorithm proposed in this research.

7. Concluding remarks

This research considers the three-dimensional descent path of a

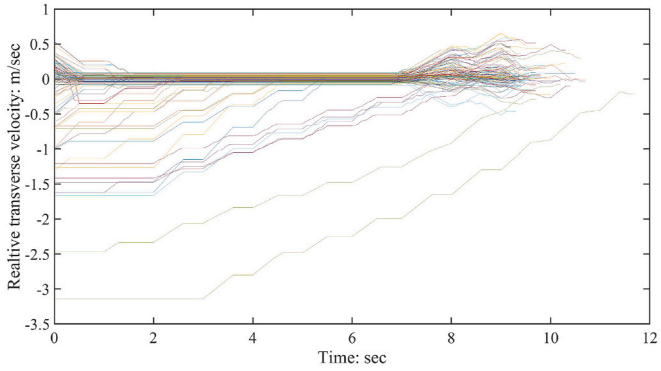

Fig. 11. Phase 2: time histories of the relative transverse velocity (MC campaign).

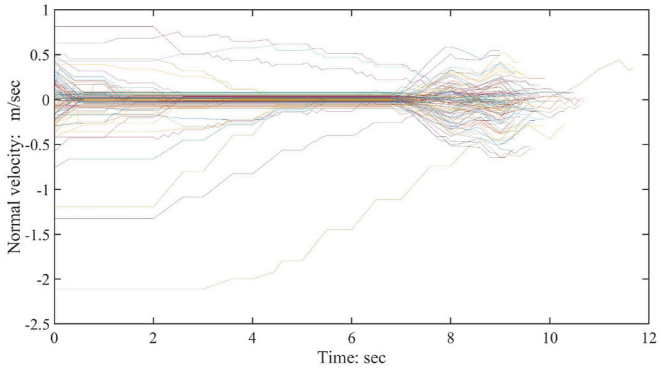

Fig. 12. Phase 2: time histories of the normal velocity (MC campaign).

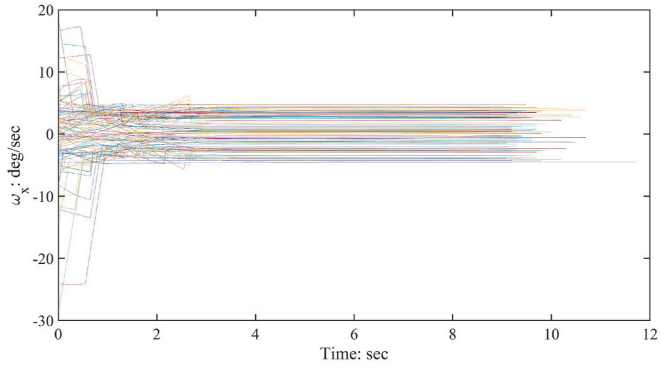

Fig. 13. Phase 2: time histories of component 1 of the angular velocity (MC campaign).

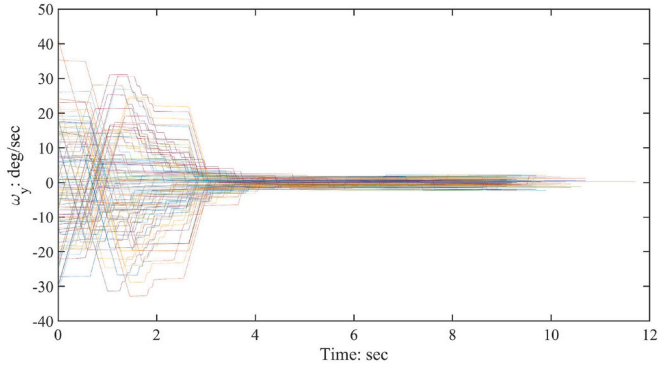

Fig. 14. Phase 2: time histories of component 2 of the angular velocity (MC campaign).

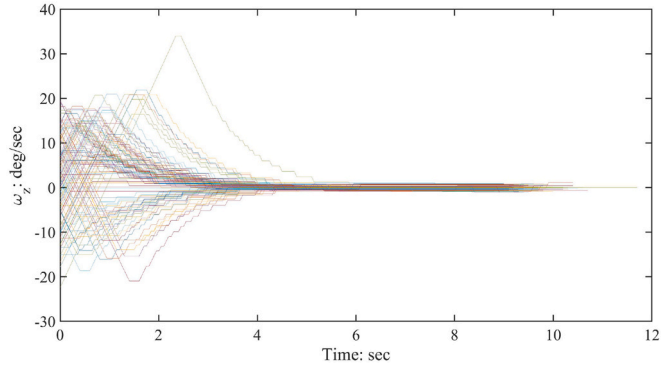

Fig. 15. Phase 2: time histories of component 3 of the angular velocity (MC campaign).

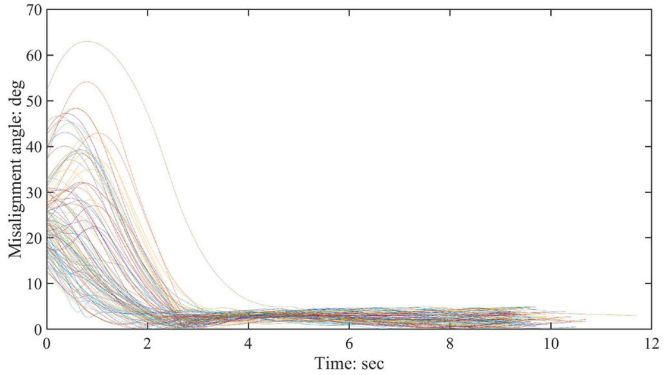

Fig. 16. Phase 2: time histories of the misalignment angle (MC campaign).

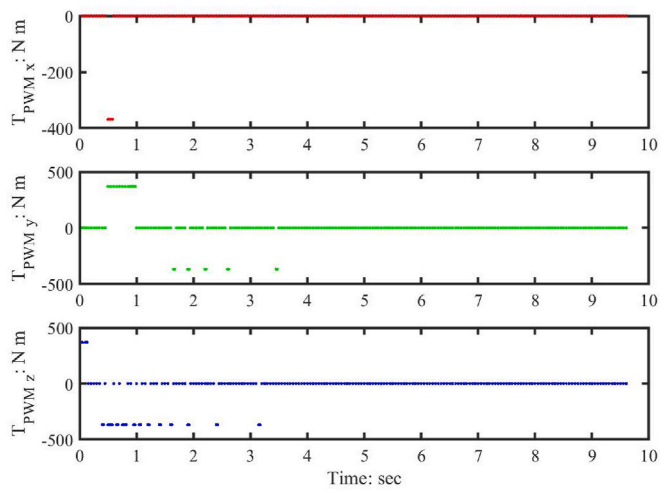

Fig. 17. Phase 2: time histories of the desired torque components yielded by PWM (single MC simulation).

spacecraft, from periselenium of its operational orbit to the lunar surface. The gravitational model includes several relevant harmonics of the selenopotential. The landing vehicle is equipped with a main propulsion system, for trajectory control, accompanied by 12 monopropellant thrusters, equally distributed into three mutually orthogonal planes and mainly dedicated to attitude maneuvering. The trajectory is split in two arcs: (1) descent trajectory, up to an altitude of 50 m, and (2) terminal approach and soft touchdown. For phase 1, a new, three-dimensional locally-flat near-optimal guidance is introduced that is based on the local projection of the position and velocity variables. A minimum-time problem is defined using the locally flat coordinates of position and velocity, and consists in

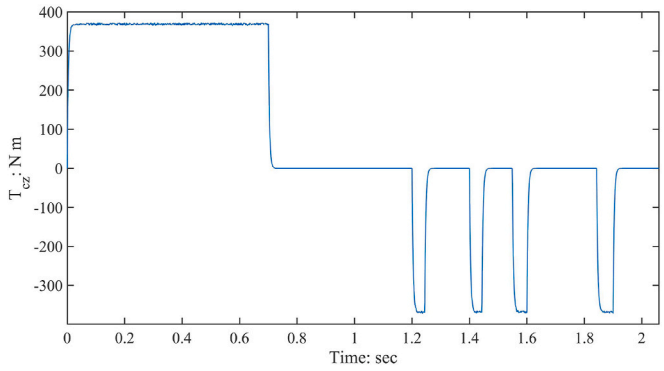

Fig. 18. Phase 2: zoom on the time history of actual torque component z (single MC simulation).

Table 3
Statistics on the final values of trajectory and attitude variables, time of flight, and final mass.

Variable	Average value	Standard deviation	Variable	Average value	Standard deviation
φ_f (deg)	– 7.4 e – 6	6.6 e – 5	φ_f (deg)	2.47	1.13
$v_{r,f}$ (m/s)	– 0.53	0.20	$\omega_{x,f}$ (deg/s)	0.50	2.78
$v_{R,t,f}$ (m/s)	6.5 e – 2	0.19	$\omega_{y,f}$ (deg/s)	8.1 e – 2	1.13
$v_{n,f}$ (m/s)	– 2.5 e – 2	0.20	$\omega_{z,f}$ (deg/s)	– 8.3 e – 2	0.48
t_f (sec)	377.0	3.8	m_f (kg)	647.8	6.6

Table 4
Statistics on the final velocity components of the four landing pads.

Average values	Pad 1	Pad 2	Pad 3	Pad 4
$v_{r,f}$ (m/s)	– 0.52	– 0.53	– 0.52	– 0.53
$v_{R,t,f}$ (m/s)	7.1 e – 2	7.5 e–2	6.5 e – 2	8.0 e – 2
$v_{n,f}$ (m/s)	– 3.4 e – 2	– 1.8 e – 2	– 2.4 e – 2	– 2.8 e – 2
Standard deviations	**Pad 1**	**Pad 2**	**Pad 3**	**Pad 4**
$v_{r,f}$ (m/s)	0.20	0.20	0.20	0.20
$v_{R,t,f}$ (m/s)	0.19	0.20	0.19	0.19
$v_{n,f}$ (m/s)	0.21	0.21	0.21	0.22

Table 5
Runtime: extremal values, average value, and standard deviation (MC campaign).

Runtime	Minimum	Maximum	Average	Standard deviation
t_{run} (sec)	230.3	269.7	247.2	6.4

finding the optimal thrust direction that minimizes the time of flight for achieving the desired conditions at the beginning of phase 2. The optimal control problem at hand is proven to be amenable to an analytical solution.

This circumstance allows translating the minimum-time problem of interest into five nonlinear equations in five unknowns. Their numerical solution can be performed as a real-time process, because a suitable guess, related to intuitive dynamical variables, is available. The method at hand yields closed-form functions of time for the two thrust angles, which identify the commanded thrust direction. The two fundamental steps of the guidance algorithm, i.e. (i) local projection and (ii) numerical solution of the nonlinear equation system, are performed iteratively, at equally-spaced sampling times. During terminal approach (phase 2), correct vertical alignment, modest vertical velocity, and zero angular rate and horizontal velocity at touchdown are pursued. With this intent, a hysteretic predictive bang-off-bang guidance algorithm is proposed that is capable of guaranteeing the desired final conditions, while providing the proper allocation of side jet ignitions. In fact, while the main thruster is employed for decelerating the landing vehicle, side jets are used for the purpose of gaining the correct attitude and simultaneously reducing the residual horizontal velocity. In both phases 1 and 2, the attitude control system has the objective of aligning the actual thrust direction, which is fixed with respect to the spacecraft, with the commanded one, provided by the guidance algorithm. Thus, for the problem at hand, attitude control must pursue single-axis alignment. This work presents and applies a new quaternion-based nonlinear reduced-attitude control algorithm, able to pursue a time-varying pointing direction. An effective feedback law identifies the required torque. The Lyapunov theorem and the LaSalle's invariance principle provide the theoretical background needed to prove that the reduced-attitude-tracking feedback law at hand enjoys asymptotic stability properties. The attitude actuation system consists of 12 mono-propellant thrusters, equally distributed into three mutually orthogonal planes. They are ignited using pulse width modulation. All the side jets are connected to the same propellant supplier and high-pressure tank, whose pressure decreases with the system actuation cycles, leading the actual torque to decrease with time. This time-varying behavior, the time delay associated with side jet switches (i.e., ignitions or shutdowns), and noise are all included in the dynamical modeling, as a further effort aimed at the accurate prediction of the overall dynamics. For the purpose of testing the guidance, control, and actuation architecture at hand, a Monte Carlo campaign is run, assuming significant displacements from the nominal initial conditions and including the most meaningful harmonics of the selenopotential. The numerical results unequivocally prove that the joint use of the two explicit guidance schemes, i.e. (a) locally-flat near-optimal guidance and (b) predictive bang-off-bang guidance, in conjunction with pulse-modulated reduced-attitude control, represents an effective approach for lunar descent and safe touchdown.

Declaration of competing interest

The authors declare that they have no known competing financial interests or personal relationships that could have appeared to influence the work reported in this paper.

Appendix. Closed-form solution for the three-dimensional locally-flat guidance

In this appendix, the optimal control problem defined by Eq. (19) is proven to be amenable to a closed-form solution. As a first step, the optimal thrust angles, written in terms of initial adjoint variables, are used in Eq. (17), leading to

$$\dot{v}_x = -\tilde{a}_T \frac{\tilde{\lambda}_{4,0} - \tilde{\lambda}_{1,0} t}{\sqrt{\left[\tilde{\lambda}_{4,0} - \tilde{\lambda}_{1,0} t\right]^2 + \left[\tilde{\lambda}_{6,0} - \tilde{\lambda}_{3,0} t\right]^2 + 1}} - g \tag{61}$$

$$\dot{v}_y = -\tilde{a}_T \frac{1}{\sqrt{\left[\tilde{\lambda}_{4,0} - \tilde{\lambda}_{1,0} t\right]^2 + \left[\tilde{\lambda}_{6,0} - \tilde{\lambda}_{3,0} t\right]^2 + 1}} \tag{62}$$

$$\dot{v}_z = -\tilde{a}_T \frac{\tilde{\lambda}_{6,0} - \tilde{\lambda}_{3,0} t}{\sqrt{\left[\tilde{\lambda}_{4,0} - \tilde{\lambda}_{1,0} t\right]^2 + \left[\tilde{\lambda}_{6,0} - \tilde{\lambda}_{3,0} t\right]^2 + 1}} \tag{63}$$

where subscript 0 refers to the initial time t_0. Because g and $\tilde{a}_T$ are constant, the preceding equations are integrable. Letting

$$c_1 = \tilde{\lambda}_{1,0}^2 + \tilde{\lambda}_{3,0}^2,\ c_2 = -2\tilde{\lambda}_{1,0}\tilde{\lambda}_{4,0} - 2\tilde{\lambda}_{3,0}\tilde{\lambda}_{6,0},\ c_3 = \tilde{\lambda}_{4,0}^2 + \tilde{\lambda}_{5,0}^2 + \tilde{\lambda}_{6,0}^2 \tag{64}$$

the general solution for Eqs. 61–63 is obtained through the Matlab symbolic toolbox [46], and is expressed in terms of elementary functions as

$$v_x(t) = v_{x,0} - g(t - t_0) + \tilde{a}_T[m_1(t) - m_1(t_0)] \tag{65}$$

$$v_y(t) = v_{y,0} + \tilde{a}_T[m_2(t) - m_2(t_0)] \tag{66}$$

$$v_z(t) = v_{z,0} + \tilde{a}_T[m_3(t) - m_3(t_0)] \tag{67}$$

where

$$m_1(t) = \frac{\tilde{\lambda}_{1,0}}{c_1}\sqrt{c_1 t^2 + c_2 t + c_3} - \frac{c_2\tilde{\lambda}_{1,0} + 2c_1\tilde{\lambda}_{4,0}}{2c_1^{3/2}} \ln\left[\frac{c_2 + 2c_1 t}{2c_1^{1/2}} + \sqrt{c_1 t^2 + c_2 t + c_3}\right] \tag{68}$$

$$m_2(t) = -\frac{1}{c_1^{1/2}} \ln\left[\frac{c_2 + 2c_1 t}{2c_1^{1/2}} + \sqrt{c_1 t^2 + c_2 t + c_3}\right] \tag{69}$$

$$m_3(t) = \frac{\tilde{\lambda}_{3,0}}{c_1}\sqrt{c_1 t^2 + c_2 t + c_3} - \frac{c_2\tilde{\lambda}_{3,0} + 2c_1\tilde{\lambda}_{6,0}}{2c_1^{3/2}} \ln\left[\frac{c_2 + 2c_1 t}{2c_1^{1/2}} + \sqrt{c_1 t^2 + c_2 t + c_3}\right] \tag{70}$$

Then, using the preceding expressions, Eq. (16) is integrated as well, to yield

$$x(t) = x_0 + \left[v_{x,0} + g t_0 - \tilde{a}_T m_1(t_0)\right](t - t_0) - \frac{1}{2} g (t - t_0)^2 + \tilde{a}_T[n_1(t) - n_1(t_0)] \tag{71}$$

$$y(t) = y_0 + \left[v_{y,0} - \tilde{a}_T m_2(t_0)\right](t - t_0) + \tilde{a}_T[n_2(t) - n_2(t_0)] \tag{72}$$

$$z(t) = z_0 + \left[v_{z,0} - \tilde{a}_T m_3(t_0)\right](t - t_0) + \tilde{a}_T[n_3(t) - n_3(t_0)] \tag{73}$$

where

$$n_1(t) = \frac{3\tilde{\lambda}_{1,0}c_2 + 4\tilde{\lambda}_{4,0}c_1 + 2\tilde{\lambda}_{1,0}c_1 t}{4c_1^2}\sqrt{c_1 t^2 + c_2 t + c_3} - \frac{\left(\tilde{\lambda}_{1,0}c_2 + 2\tilde{\lambda}_{4,0}c_1\right)(c_2 + 2c_1 t)}{4c_1^{5/2}} \ln\left[\frac{c_2 + 2c_1 t}{2c_1^{1/2}} + \sqrt{c_1 t^2 + c_2 t + c_3}\right] \tag{74}$$

$$n_2(t) = \frac{\sqrt{c_1 t^2 + c_2 t + c_3}}{c_1} - \frac{c_2 + 2c_1 t}{2c_1^{3/2}} \ln\left[\frac{c_2 + 2c_1 t}{2c_1^{1/2}} + \sqrt{c_1 t^2 + c_2 t + c_3}\right] \tag{75}$$

$$n_3(t) = \frac{3\tilde{\lambda}_{3,0}c_2 + 4\tilde{\lambda}_{6,0}c_1 + 2\tilde{\lambda}_{3,0}c_1 t}{4c_1^2}\sqrt{c_1 t^2 + c_2 t + c_3} - \frac{\left(\tilde{\lambda}_{3,0}c_2 + 2\tilde{\lambda}_{6,0}c_1\right)(c_2 + 2c_1 t)}{4c_1^{5/2}} \ln\left[\frac{c_2 + 2c_1 t}{2c_1^{1/2}} + \sqrt{c_1 t^2 + c_2 t + c_3}\right] \tag{76}$$

Equations (65)–(67) and (71)-(73), in conjunction with Eqs. (68)–(70) and (74)-(76), provide the time histories of $\{x, y, z, v_x, v_y, v_z\}$. They can be written in the compact form (32) and evaluated at the final time. In the context of the near optimal locally-flat guidance, the initial time t_0 is the instant t_k when the sampling interval $[t_k, t_{k+1}]$ begins.

References

[1] A.R. Klumpp, Apollo Guidance, Navigation and Control: Apollo Lunar Descent Guidance, Massachusetts Institute of Technology, Charles Stark Draper Lab., TR-R695, Cambridge, MA, 1971.

[2] G.W. Cherry, E-Guidance – A General Explicit, Optimizing Guidance Law for Rocket-Propelled Spacecraft, " Massachusetts Institute of Technology, Cambridge (MA), USA, 1964. Report 456.

[3] S. Nemeth, "Revisiting Apollo: Lunar Landing Guidance,", in: AIAA-Houston Annual Technical Symposium, Houston (TX), USA, 2006.

[4] D. Azimov, Enhanced apollo-class real-time targeting and guidance for powered descent and precision landing, in: AIAA Guidance, Navigation, and Control (GNC) Conference, 2013. Boston (MA), USA.

[5] C.T. Chomel, R.H. Bishop, Analytical lunar descent guidance algorithm, J. Guid. Control Dynam. 32 (No. 3) (2009) 915–926.

[6] D.M. Azimov, R.H. Bishop, Integrated targeting and guidance for powered planetary descent, J. Astronaut. Sci. 65 (No. 2) (2018) 229–259.

[7] A.Y. Lee, Fuel-efficient descent and landing guidance logic for a safe lunar touchdown, in: AIAA Guidance, Navigation and Control Conference, OR, Portland, 2011. AIAA Paper 2011–6499.

[8] T.P. Reynolds, M. Mesbahi, Optimal planar powered descent with independent thrust and torque, J. Guid. Control Dynam. 43 (No. 7) (2020) 1225–1231.

[9] X. Jiang, R. Furfaro, Integrated guidance for Mars entry and powered descent using reinforcement learning and pseudospectral method, Acta Astronaut. 163 (2019) 114–129. Part B.

[10] D.G. Hull, Optimal guidance for quasi-planar lunar descent with throttling, Adv. Astronaut. Sci. 140 (2011) 983–994. Paper AAS 11-169.

[11] F. Zhang, G.R. Duan, Integrated translational and rotational control for the terminal landing phase of a lunar module, Aero. Sci. Technol. 27 (2013) 112–126.

[12] L. Ma, Z. Shao, W. Chen, Z. Song, Trajectory optimization for lunar soft landing with a Hamiltonian-based adaptive mesh refinement strategy, Adv. Eng. Software 100 (2016) 266–276.

[13] S. Mathavaraj, R. Pandiyan, R. Pandhi, Optimal trajectory planning for multiphase lunar landing, IFAC-PapersOnLine 49 (1) (2016) 124–129.

[14] R. Cortés-Martínez, K.D. Kumar, H. Rodríguez-Cortés, Precise power descent control of a lunar lander using a single thruster, Acta Astronaut. 186 (2021) 473–485.
[15] B.I. Zhukov, V.N. Likhachev, Y.G. Sikharulidze, An algorithm for safe landing of a spacecraft during descent from a circumlunar orbit, Cosmic Res. 60 (2022) 347–357.
[16] A.W. Berning, L. Strohl, S.R. Bieniawski, "Lossless Convex Guidance for Lunar Powered Descent,", in: AIAA SciTech 2023 Forum, National Harbor, MD, 2023. AIAA Paper 2023-2004.
[17] B. Tian, W. Fan, R. Su, Q. Zong, Real-time trajectory and attitude coordination control for reusable launch vehicle in reentry phase, IEEE Trans. Ind. Electron. 62 (No. 3) (2015) 1639–1650.
[18] B. Tian, W. Fan, Q. Zong, Integrated guidance and control for reusable launch vehicle in reentry phase, Nonlinear Dynam. 80 (2015) 397–412.
[19] T.A. Ely, M. Heyne, J.E. Riedel, Altair navigation performance during translunar cruise, lunar orbit, descent, and landing, J. Spacecraft Rockets 49 (No. 2) (2012) 295–317.
[20] D.K. Geller, D.P. Christensen, Linear covariance analysis for powered lunar descent and landing, J. Spacecraft Rockets 46 (No. 6) (2009) 1231–1248.
[21] X. Jiang, T. Tao, Guidance summary and assessment of the Chang'e-3 powered descent and landing, J. Spacecraft Rockets 53 (No. 2) (2016) 258–277.
[22] C. Bai, J. Guo, H. Zheng, Optimal guidance for planetary landing in hazardous terrains, IEEE Trans. Aero. Electron. Syst. 56 (No. 4) (2020) 2896–2909.
[23] H. Zhao, H. Dai, Z. Dang, Optimal guidance for lunar soft landing with dynamic low-resolution image sequences, Adv. Space Res. 69 (No. 11) (2022) 4013–4025.
[24] N.A. Chaturvedi, A.K. Sanyal, N.H. McClamroch, Rigid-body attitude control, IEEE Control Syst. Mag. 31 (No.3) (2011) 30–51.
[25] C.M. Pong, D.W. Miller, Reduced-attitude boresight guidance and control on spacecraft for pointing, tracking, and searching, J. Guid. Control Dynam. 38 (No. 6) (2015) 1027–1035.
[26] Q. Hu, B. Chi, M.R. Akella, Reduced attitude control for boresight alignment with dynamic pointing constraints, IEEE ASME Trans. Mechatron. 24 (No. 6) (2019) 2942–2952.
[27] Y. Silik, U. Yaman, Single Axis attitude controller design using pulse width modulated thruster, in: 20th International Conference on Research and Education in Mechanics (REM), 2019. Wels, Australia,.
[28] R.N. Knauber, Roll torques produced by fixed-nozzle solid rocket motors, J. Spacecraft Rockets 33 (No. 6) (1996), 789–485.
[29] K.H. Kienitz, J. Bals, Pulse modulation for attitude control with thrusters subject to switching restrictions, Aero. Sci. Technol. 9 (2005) 635–640.
[30] M. Pontani, F. Celani, S. Carletta, Explicit Near-Optimal Guidance and Pulse-Modulated Control for Lunar Descent and Touchdown, Aerotecnica Missili & Spazio, 2022 online 13 August.
[31] Astrobotic Peregrine, Lunar Lander User's Guide, Vers 4.0, 2020.
[32] J.C. Dutton, R.E. Coverdill, Experiments to study the gaseous discharge and filling of vessels, International Journal of. Engineering Education 13 (No. 2) (1997) 123–134.
[33] G. Artingstall, Displacement of Gas from a Ruptured Container and its Dispersal in the Atmosphere, vol. 33, Institution of Chemical Engineering Symposium Series, 1972, pp. 3–6.
[34] P.C. Hughes, Spacecraft Attitude Dynamics, Dover Publications, Inc., Mineola, 2004, pp. 55–61.
[35] F.R. William, Apollo Experience Report Lunar Module Landing Gear Subsystem, NASA TN D-6850, Houston, TX, 1972.
[36] M. Pontani, G. Cecchetti, P. Teofilatto, Variable-time-domain neighboring optimal guidance applied to space trajectories, Acta Astronaut. 115 (2015) 102–120.
[37] K.D. Mease, D.T. Chen, P. Teufel, H. Schonenberger, Reduced-order entry trajectory planning for acceleration guidance, J. Guid. Control Dynam. 25 (2002) 607–615.
[38] Y.E. Arslantaş, T. Oehlschlägel, M. Sagliano, Safe landing area determination for a Moon lander by reachability analysis, Acta Astronaut. 128 (2016) 607–615.
[39] D.G. Hull, Optimal Control Theory for Applications, Springer, New York, 2003, pp. 199–254.
[40] F.M. Perkins, Explicit tangent-steering guidance for multi-stage boosters, Astronaut. Acta 12 (1966) 212–223.
[41] I.E. Smith, General formulation of the iterative guidance mode, NASA TM X-53414, 1966.
[42] R.G. Brusch, Bilinear tangent yaw guidance, in: Guidance and Control Conference, 1979. Boulder.
[43] H. Weiss, Quaternion-based rate/attitude tracking system with application to gimbal attitude control, J. Guid. Control Dynam. 16 (4) (1993) 609–616.
[44] W.M. Haddad, V. Chellaboina, Nonlinear Dynamical Systems and Control: A Lyapunov-Based Approach, Princeton University Press, 2008, p. 285.
[45] Flight-Proven High Performance Green Propulsion, 200N HPGP Thruster, Bradford Ecaps, Solna, Sweden, 2020. https://www.ecaps.space/products-200n.php.
[46] Symbolic Math Toolbox – User's Guide, The MathWorks, Inc. 1 Apple Hill Drive, Natick, MA, 2023.